



Title	Form drag in quasigeostrophic flow over sinusoidal topography
Author(s)	Uchimoto, Keisuke
Citation	北海道大学. 博士(地球環境科学) 甲第6986号
Issue Date	2004-06-30
DOI	10.14943/doctoral.k6986
Doc URL	http://hdl.handle.net/2115/47708
Type	theses (doctoral)
File Information	uchimoto.pdf



[Instructions for use](#)

Form drag in quasigeostrophic flow over sinusoidal topography

KEISUKE Uchimoto

Division of Ocean and Atmospheric Science
Graduate School of Environmental Earth Science, Hokkaido University

April, 2004

abstract

The relationship between form drag and the zonal mean velocity in steady states is investigated in a very simple system, a barotropic quasi-geostrophic β channel with a sinusoidal topography. When a steady solution is calculated by the modified Marquardt method keeping the zonal mean velocity constant as a control parameter, the characteristic of the solution changes at a velocity. The velocity coincides with a phase speed of a wave whose wavenumber is higher than that of the bottom topography. For smaller than this critical velocity, a stable quasi-linear solution which is similar to the linear solution exists. For larger than the critical velocity, three solutions whose form drag is very large exist which extend from the stable quasi-linear solution. It is inferred from the linear solution that these changes of the solution is due to the resonance of higher modes than that of the bottom topography. It is also found that the resonant velocity of the mode whose wavenumber is the same as the bottom topography has no effect on these solutions. When the quiescent fluid is accelerated by a constant wind stress, the acceleration stops around the critical velocity for wide range of the wind stress. If the wind stress is too large for the acceleration to stop there, the zonal current speed continues to increase infinitely. It is implied that the zonal velocity of equilibrium is mainly determined not by the wind stress but by the amplitude of the bottom topography and the viscosity coefficient. This implies that the zonal mean velocity does not change very much when the winds change.

Contents

abstract	i
1 Introduction	1
2 Model and Methodology	6
2.1 Model description	6
2.2 Numerical calculations and experiments	8
2.3 Form drag instability	9
3 Steady solutions	11
3.1 Approximate solutions	12
3.2 Low-order Models	13
3.2.1 $(N, M) = (1, 3)$ case	13
3.2.2 $(N, M) = (1, 7)$ case	15
3.2.3 Resonance of a higher mode	16
3.2.4 Summary	19
3.3 High-order Models	20
4 Numerical experiments	24
5 Summary and Discussion	31
Acknowledgments	36

Appendix	37
A. the linear stability analysis	37
B. the Levenberg-Marquardt-Morrison method	38
References	40
Figures	43

Chapter 1

Introduction

The Southern Ocean is an important region both in terms of the earth's climate and in terms of the dynamics of currents because of the absence of land barriers in the latitude band of the Drake Passage.

About 71 percent of the earth's surface is covered with the ocean, and almost 90 percent of the ocean is occupied by the three major oceans, the Pacific, the Atlantic and the Indian Oceans. The Southern Ocean combines the three and makes it possible to exchange water between them. For example, the deep watermass formed in the high-latitude North Atlantic, called the North Atlantic Deep Water, flows southward, and in the Southern Ocean it is transported eastward into the Pacific and the Indian Oceans. In addition to the water exchange between the three major oceans, the Southern Ocean influences the climate through the meridional overturning. No net southward geostrophic flow can exist in the latitude band of the Drake Passage since there is no net zonal pressure gradient. This limits the heat transport across the latitude band.

The Southern Ocean is unique in its dynamics. There exists the strong eastward flow driven by the westerly wind, which is called the Antarctic Circumpolar Current (ACC). It is one of the strongest currents in the world. Besides the ACC, strong currents exist in the Ocean, which flow near western boundaries of the zonally bounded oceans: the western boundary currents. The dynamics of the ACC and the western boundary currents is quite different. The western boundary currents are a part of the wind-driven circulations in the

zonally bounded oceans. The fundamental dynamics of the circulation was elucidated by Sverdrup (1947). It is called the Sverdrup dynamics after him. The dynamics is governed by the vorticity. The meridional flow in the interior is northward or southward depending on the curl of the wind stress, and to satisfy the mass conservation, the meridional flow opposite to the interior flow exists in the narrow western boundary layer (Stommel, 1948; Munk, 1950), which is the western boundary current. The keystone is not the wind stress itself but the curl of the wind. Therefore the directions of the winds and the currents in the oceans are not always same.

The ACC is, on the other hand, thought to be driven by the westerly wind stress itself, not by the curl of the wind stress, and the current flows eastward. The dynamics of the current which flows in the same direction as the winds seems easier, but actually the dynamics of the ACC has been problematic. There exists a fundamental problem known as Hidaka's dilemma. When the transport is calculated in a zonal channel with a flat bottom, it becomes much larger than the observed value or unrealistically large eddy coefficients are needed for the transport to be a reasonable value (Hidaka and Tsuchiya, 1953). The problem is what removes the momentum which is imparted by the winds.

An idea suggested by Munk and Palmén (1951) is most acceptable now. Munk and Palmén (1951) proposed that the bottom form drag balances the winds. It was difficult to ascertain it at that time since it was impossible neither to observe accurately enough to calculate the balance nor to conduct numerical experiments. But as abilities and capacities of the computer have highly developed, many numerical experiments with eddy-resolving quasigeostrophic models (for example, McWilliams *et al.*, 1978; Treguier and McWilliams, 1990 ; Wolf *et al.*, 1991) and with primitive models (for example, FRAM Group, 1991; Klinck, 1992; Gille, 1997) have been performed in the last quarter of a century. These results showed the balance between the winds and the bottom form drag. This is rephrased from the point of view of meridional overturning as that the northward Ekman transport by the westerly winds returns as geostrophic flow across the latitude

band of the Drake Passage (Fig. 1). Net southward geostrophic transports are possible in the zonally unbounded ocean if the bottom is not flat. Actual meridional overturning is, of course, not so simple as Fig. 1. For example, Speer *et al.* (2000) discussed the meridional flow in the Southern Ocean.

Despite of the results of the numerical experiments, some oceanographers think the transport of the ACC is determined by the Sverdrup dynamics, not by the balance between the wind stress and the bottom form drag. This idea was first proposed by Stommel (1957). Warren *et al.* (1996) recently asserted this idea and denied the idea of the bottom form drag. Warren *et al.* (1996) insisted that the equation expressing the balance between the wind stress and the form drag is independent of the transport and that it just states meridional circulation. Olbers (1998) argued against Warren *et al.* (1996) theoretically and the recent numerical experiments performed by Tansley and Marshall (2001) did not support the Sverdrup dynamics.

Studies on the transport of the ACC have been developed and getting more complicated. Gnanadesikan and Hallberg (2000), for example, suggests that thermodynamics as well as dynamics is important. Form drag is, however, not understood well. Even one of the most fundamental problems remains to be solved: when the wind stress balances the form drag, how much can the transport be? We revisit this basic problem. The form drag is expressed as

$$\iint \eta \frac{\partial \psi}{\partial x} dx dy,$$

where ψ is geostrophic stream function, and η is bottom topography. Although actually the form drag depends on the transport through ψ , apparently it is independent of the transport and therefore the relation with the transport is hard to understand. In the present study, we investigate the relation between the transport and the wind stress in a simple system, a homogeneous quasigeostrophic β channel with a sinusoidal bottom topography. We do not consider the bottom friction and chose the free slip condition on the walls of the channel, so that the zonal momentum sink is only the bottom form drag

in the system (see Section 2.1 for details on the model).

These quasigeostrophic β channels have been used, especially in 1980's, mainly in studies of meteorological phenomena such as the blocking. A pioneer work was done by Charney and DeVore (1979), who investigated the multiple flow equilibria in quasigeostrophic barotropic fluid over the sinusoidal bottom topography, and found the existence of multiple equilibria. They also showed that the form drag instability, which is generated by the interaction between the flow and the bottom topography, is important for transition between the two steady solutions. While Charney and DeVore (1979) used a severely truncated low-order model, Pedlosky (1981) treated a similar problem by a weakly nonlinear theory. Yoden (1985) investigated bifurcation properties of a nonlinear system, extended version of the Charney and DeVore system. Mukougawa and Hirota (1986) studied linear stability properties of the inviscid exact steady solution over the bottom topography. Rambaldi and Mo (1984) showed that multiple equilibria are not artificially introduced by the severe truncation. Recently, Tian *et al.* (2001) have conducted laboratory and numerical experiments and showed the existence of multiple equilibria, the blocked and the zonal flow. The baroclinic systems have also been studied (e.g., Charney and Strauss, 1980; Pedlosky, 1981).

The model used in the present study is the same as that in Rambaldi and Mo (1984) saving the dissipation. We use a lateral Laplacian diffusion as a dissipation while Rambaldi and Mo (1984) used a bottom friction. This difference arises from the object; their object is the atmosphere and our object is the ocean. In the oceans, the horizontal diffusion by turbulent eddies is thought to be more important than the bottom Ekman friction for large scale motions. When horizontal diffusion is used, higher modes would work effectively for the form drag. And the higher the wavenumber of the mode becomes, the more effectively the mode is damped. Therefore we can anticipate different results originated from the difference in the dissipation. If we take a Laplacian diffusion in the vorticity equation, $A_H \nabla^4 \psi$, where A_H is the viscosity coefficient, ∇ is the horizontal gradient operator and ψ

is the geostrophic stream function in a barotropic quasigeostrophic model (see (2.1) and (2.4) in section 2.1), the energy equation for steady state yields

$$\iint U\tau dx dy = - \iint U\eta \frac{\partial\psi}{\partial x} dx dy = \iint A_H (\nabla^2\psi)^2 dx dy,$$

where U is the mean eastward velocity and the wind stress τ is assumed to be spatially constant. This equation suggests that the form drag can be significant when the higher mode coefficients are large, even if A_H is small. The zonal mean velocity where a higher mode is amplified may be different from the resonant velocity with the bottom topography. If so, the form drag can also be amplified at the point, different from the resonance with the bottom topography, which would be thought to play an important role in this system.

The system we consider is so simple that the results are difficult to be applied directly to the real circumpolar current. But the relation between the magnitude of the form drag and the current velocity in a nonlinear system is an interesting subject in geophysical fluid dynamics. The present study can be a step towards a better understanding of the interactions between flow and topography.

The remainder of this paper is organized as follows; the model is formulated in Chapter 2. The steady solutions are shown in Chapter 3. The results of numerical experiments are shown in Chapter 4. The summary and discussion of this study are provided in Chapter 5.

Chapter 2

Model and Methodology

2.1 Model description

We consider a barotropic quasigeostrophic flow contained within a zonally oriented periodic β -channel. The nondimensional width and length of the channel are π , respectively (Fig.2). The nondimensional quasigeostrophic potential vorticity equation for barotropic fluid is

$$\frac{\partial \nabla^2 \psi}{\partial t} + J(\psi, \nabla^2 \psi + \beta y + \eta) = -\frac{\partial \tau}{\partial y} + A_H \nabla^4 \psi, \quad (2.1)$$

where ψ is the geostrophic stream function whose x and y derivatives give v and $-u$ respectively, t time, ∇^2 horizontal Laplacian, β the latitudinal variation of Coriolis parameter, the value of which we will set $1/\pi$, η height of the bottom topography, A_H the horizontal diffusion coefficient and τ the zonal wind stress. $J(a, b)$ is horizontal Jacobian: $J(a, b) \equiv \frac{\partial a}{\partial x} \frac{\partial b}{\partial y} - \frac{\partial a}{\partial y} \frac{\partial b}{\partial x}$. In order to highlight the effect of the bottom form drag, we consider as simple a condition as possible;

- the wind stress, τ , is constant and westerly: $\frac{\partial \tau}{\partial y} = 0$, and $\tau > 0$, and
- the bottom topography consists of a single wave: $\eta = \eta_0 \sin 2x \sin y$.

While our interest is in the transport, in the barotropic model the transport is proportional to the zonal mean velocity, U , which is,

$$U = \frac{1}{S} \int_0^\pi \int_0^\pi \left(-\frac{\partial \psi}{\partial y} \right) dx dy,$$

where $S = \pi^2$ is the area of the channel. Therefore we rewrite ψ as

$$\psi(x, y, t) = -U(t)y + \phi(x, y, t),$$

where ϕ is a stream function which has no contribution to the zonal mean velocity. Then (2.1) is rewritten as

$$\frac{\partial \nabla^2 \phi}{\partial t} + J(-Uy + \phi, \nabla^2 \phi + \beta y + \eta) = A_H \nabla^4 \phi. \quad (2.2)$$

The boundary conditions on the southern and the northern walls are free slip conditions, that is,

$$\phi = 0 \quad \text{and} \quad \nabla^2 \phi = 0 \quad \text{at} \quad y = 0, \pi. \quad (2.3)$$

Since the channel is periodic,

$$\phi(x, y, t) = \phi(x + \pi, y, t).$$

In a multiply connected domain such as the present channel, the stream function, ψ , is not completely determined by the quasigeostrophic equation (2.1) alone. In the present case, the value of the stream function on the southern wall can be set 0 without any loss of generality, but the value of the stream function on the northern wall, $\psi(x, \pi, t) = -U(t)\pi$, is not determined. As shown by McWilliams (1977), supplementary conditions are necessary. In the present case, one condition,

$$\frac{dU}{dt} = \frac{1}{S} \int_0^\pi \int_0^\pi \eta \frac{\partial \psi}{\partial x} dx dy + \tau, \quad (2.4)$$

is needed. In deriving (2.4), the boundary condition (2.3) and the assumption that τ is constant are used. This is the zonal momentum equation averaged by the channel area, and means that the momentum source is the wind stress, τ , and that the sink is only the bottom form drag, the first term on the right-hand side of (2.4), for the bottom friction is neglected. The viscous term is not contained in (2.4) due to the free slip boundary condition on the walls. This, however, does not mean that the dissipation is unimportant. The form drag results from the pressure being out of phase with respect to the bottom topography. The dissipation in (2.2) is responsible for it.

2.2 Numerical calculations and experiments

Numerical calculations are carried out in spectral forms of (2.2) and (2.4). To obtain the spectral forms, we expand ϕ in orthogonal functions as follows:

$$\phi = \sum_{m=1}^M \sum_{n=1}^N \phi_{2nm} + \sum_{m=1}^M \phi_{0m} \quad (2.5)$$

$$\text{where } \begin{cases} \phi_{2nm} = (A_{2nm} \cos 2nx + B_{2nm} \sin 2nx) \sin my \\ \phi_{0m} = Z_m \sin my \end{cases}$$

which satisfy the boundary condition (2.3). When they are substituted into (2.2) and (2.4), $(2 \times N + 1) \times M + 1$ equations for A_{2nm} , B_{2nm} , Z_m and U are obtained. Jacobian is, however, calculated at grid points in physical space and then it is expanded to the orthogonal functions. The form drag term, $\frac{1}{S} \iint \eta \frac{\partial \psi}{\partial x} dx dy$, becomes $-\frac{1}{2} \eta_0 A_{21}$ due to the orthogonal relation of the trigonometric function since $\eta = \eta_0 \sin 2x \sin y$ in the present study. Hereafter a mode with a wavenumber $(2n, m)$ ($n = 0, 1, 2, \dots, N; m = 1, 2, \dots, M$), ϕ_{2nm} , is referred to as the $(2n, m)$ mode. The phase velocity is

$$C_{2nm} = -\frac{\beta}{(2n)^2 + m^2} \quad (n \neq 0). \quad (2.6)$$

Firstly we discuss the steady solution in the next chapter although our concern is to know the zonal mean velocity, U , in the equilibrium when the initially quiescent fluid is accelerated by the constant westerly wind. We treat the zonal mean velocity, U , as a control parameter and numerically solve the transformed equations of

$$J(-Uy + \phi, \nabla^2 \phi + \beta y + \eta) = A_H \nabla^4 \phi. \quad (2.7)$$

The linear stability properties of the obtained steady solutions are also examined. The method of the linear stability analysis is outlined in Appendix A. Since (2.4) reduces to

$$\tau = -\frac{1}{S} \int_0^\pi \int_0^\pi \eta \frac{\partial \psi}{\partial x} dx dy = \frac{1}{2} \eta_0 A_{21} \quad (2.8)$$

for steady flow, we can know the wind stress, τ , corresponding to the obtained steady solution by calculating the right-hand side of (2.8). The method used to calculate a steady so-

lution is the modified Marquardt method (Levenberg-Marquardt-Morrison method; hereafter referred to as LMM). The LMM is outlined in Appendix B (see also the Appendix of Yoden, 1985). The LMM necessitates an initial guess, on which the obtained steady solution depends. Solutions obtained by the LMM are *near* (similar) ones to the initial guess. The initial guess we mainly use is the inviscid exact solution. Besides those, we use the obtained steady solution as the initial guess, and follow the branch of the steady solution changing the value of the control parameter U .

Secondly we perform numerical experiments in which the zonal mean velocity, U , is permitted to vary, that is, the equations (2.2) and (2.4) are both calculated in the experiments. Initial conditions are at rest. Our main concern is whether the acceleration of the zonal mean velocity stops, and when it stops, whether the time-dependent solution approaches and converges into a stable steady solution if it is obtained by the LMM.

Since $U \frac{\partial \eta}{\partial x}$ acts as the forcing term in the potential vorticity equation (2.2), the (2, 1) mode whose wavenumber is same as the bottom topography is directly excited. It is convenient to introduce a normalized zonal mean velocity U_N defined as

$$U_N = \frac{U}{|C_{21}|}, \quad (2.9)$$

where C_{21} is the phase velocity of the (2, 1) mode. In the following discussions, we use U_N for the zonal mean velocity. Similarly, the normalized phase speed, $|C_{2nm}|_N$, is introduced as

$$|C_{2nm}|_N = \frac{|C_{2nm}|}{|C_{21}|}. \quad (2.10)$$

2.3 Form drag instability

A stable solution when the zonal mean velocity U is constant is not always stable when U is permitted to vary. Therefore a solution of the numerical experiment do not always converge into a steady solution which is stable when U is constant.

For example, there is an instability known as the form drag instability. It is easily

decided whether a solution is stable or unstable to the form drag instability without solving an eigenvalue problem as is normally done (Tung and Rosenthal,1985; and Tung and Rosenthal, 1986). We outline it in this section.

Equation (2.2) can be rewritten symbolically as

$$\frac{dU_N}{dt} = \tau_0 - D(U_N) \quad (2.11)$$

where τ_0 is the given wind stress and D is the form drag. We assume that there is $U_N = U_{N0}$ satisfying $\tau_0 - D(U_{N0}) = 0$. This U_{N0} gives the steady solution. The stability characteristic of this solution can be obtained by considering a perturbation of U_N , i.e., $U_N = U_{N0} + u'$. Then (2.11) becomes

$$\frac{du'}{dt} = \tau_0 - D(U_{N0} + u') \simeq \tau_0 - D(U_{N0}) - \left. \frac{dD}{dU_N} \right|_{U_{N0}} u' = - \left. \frac{dD}{dU_N} \right|_{U_{N0}} u' \quad (2.12)$$

Therefore, if $\left. \frac{dD}{dU_N} \right|_{U_{N0}} < 0$, the solution is unstable, that is, the solution whose form drag becomes small with the increase of U is unstable to the form drag instability.

Chapter 3

Steady solutions

In this chapter, steady solutions are discussed. In the first place, two approximate solutions in this system are shown: the inviscid exact solution and the linear solution. Next, the steady solutions in nonlinear systems are discussed. Firstly, in section 3.2, we discuss steady solutions in low-order models which are nonlinear but with severe truncation in the orthogonal expansion, (2.5). Such a simple system gives us a clear image on the dynamics. Secondly, in section 3.3, steady solutions in a high-order model in which the truncation number, M and N in (2.5), is large enough that it does not effect a drastic change in the solution are discussed. Steady solutions in these models are calculated with the LMM by using the zonal mean velocity, U_N , as the control parameter. The steady solution discussed first is the quasi-linear solution which is near the linear solution. It will be obtained by using the inviscid exact solution as the initial guess in the LMM. Besides, some other solutions are discussed.

It is known that there exist two kinds of modes in this system: an even mode and an odd mode (Yoden, 1985; called S-mode and T-mode). If $\exp(i2nx) \sin my$ satisfies $m + n = \text{even}$, it is an even mode. Otherwise it is an odd mode. Interactions between even modes make only even modes. As the bottom topography, $\eta = \eta_0 \sin 2x \sin y$, is an even modes in the present study, no odd modes appear theoretically if the quiescent fluid is accelerated by a constant wind stress. Actually computational errors in numerical integrations make very small odd modes, and they grow when the solution is unstable

to odd modes. Therefore steady solutions consisting of only even modes are mainly calculated in this section, but the linear stability of the obtained solutions is studied both to even modes and to odd modes.

3.1 Approximate solutions

As the exact steady solution of (2.2) cannot be analytically obtained in general, (2.2) is solved numerically with the LMM. Before discussing solutions calculated by the LMM, we introduce two approximate solutions to (2.2).

One is the inviscid exact solution. Since very small A_H is considered in the present study, (2.2) might be approximated to

$$J(-Uy + \phi, \nabla^2 + \beta y + \eta) \approx 0. \quad (3.1)$$

It is well known that there exists an exact steady solution $\phi^{(I)}$ of (3.1),

$$\begin{aligned} \phi^{(I)} &= B_{21}^{(I)} \sin 2x \sin y, \\ \text{where } B_{21}^{(I)} &= \frac{\eta_0}{5(U - |C_{21}|)} \end{aligned} \quad (3.2)$$

(for example, Mukougawa and Hirota, 1986), where C_{21} is defined in (2.6).

The other is a linear solution, which is obtained by considering only the (2, 1) mode, same mode as the bottom topography. The linear solution is

$$\begin{aligned} \phi^{(L)} &= \left(A_{21}^{(L)} \cos 2x + B_{21}^{(L)} \sin 2x \right) \sin y, \\ \text{where } \begin{cases} A_{21}^{(L)} &= \frac{50A_H\eta_0U}{(25A_H)^2 + 4\{5(U - |C_{21}|)\}^2}, \\ B_{21}^{(L)} &= \frac{4\eta_0U\{5(U - |C_{21}|)\}}{(25A_H)^2 + 4\{5(U - |C_{21}|)\}^2}. \end{cases} \end{aligned} \quad (3.3)$$

The form drag of the linear solution is

$$-\frac{1}{2}\eta_0 A_{21}^{(L)} = -\frac{25A_H\eta_0^2U}{(25A_H)^2 + 4\{5(U - |C_{21}|)\}^2}. \quad (3.4)$$

As A_H is very small in the present study, the difference between $B_{21}^{(I)}$ and $B_{21}^{(L)}$ is very little.

The inviscid exact solution $\phi^{(L)}$ becomes infinity and the linear solution $\phi^{(L)}$ becomes huge at $U = |C_{21}|$, which is the resonance with the bottom topography. This implies that these are not approximate solutions to the solution of (2.2) when $U \approx |C_{21}|$, for the nonlinear terms cannot be neglected. However, the critical U beyond which these solutions fail to approximate to the solution of (2.2) is not known.

3.2 Low-order Models

In this subsection, we show solutions of two low-order models. One is the case with $(N, M) = (1, 3)$ in (2.5), which includes minimum nonlinear terms, and the other is the case with $(N, M) = (1, 7)$.

At least when U_N is much smaller than $|C_{21}|_N$, the inviscid exact solution is thought to be approximate solution as stated above. The calculation using the inviscid exact solution as the initial guess in the LMM is carried out from $U_N \approx 0$ (when $U_N = 0$, the solution is $\phi = 0$) to $U_N \approx 1.0$ (when $U_N = 1.0$, the inviscid exact solution disappears). The following discussion and the figures are mainly only for $0 < U_N < 0.6$ since the stable quasi-linear solution was not obtained for $U_N > 0.6$.

3.2.1 $(N, M) = (1, 3)$ case

When $(N, M) = (1, 3)$, the modes included are ϕ_{21} , ϕ_{23} , ϕ_{02} , ϕ_{22} , ϕ_{01} , and ϕ_{03} , the first three of which are even modes and the last three of which are odd modes.

Figure 3 shows the form drag of the obtained steady solution when $(\eta_0, A_H) = (0.1, 3.0 \times 10^{-5} \pi^2)$. The value of the form drag is normalized by that of the linear solution (3.4), i.e., the normalized form drag is $A_{21}/A_{21}^{(L)}$. The vertical axis is a logarithmic coordinate. A stable solution is plotted by an open circle, \circ , a solution unstable to even modes by an asterisk, $*$, and a solution stable to even modes but unstable to odd modes by an open triangle, \triangle . We obtain the solution whose form drag is near unity using the inviscid exact solution (3.1) as the initial guess, and obtain the solution whose form drag is far larger

than the linear one extending the stable quasi-linear solution.

A striking and important feature is that a stable quasi-linear solution is obtained only for $U_N \lesssim |C_{23}|_N$ and that the steady quasi-linear solution obtained for $U_N > |C_{23}|_N$ is all unstable. This means that the critical U_N beyond which the stable quasi-linear solution is not obtained is $|C_{23}|_N (\approx 0.38)$, i.e., the phase speed of a higher mode than the (2, 1) mode which is the same mode as the bottom topography. Although the magnitude of the form drag depends on A_H and η_0 , the qualitative feature is insensitive to them at least A_H is not much larger than the value adopted here. Figure 4 shows that. Contours in Fig. 4 denotes the form drag of the quasi-linear solution stable to even modes. The value of the form drag is normalized by that of the linear one. The solution whose normalized form drag is equal to or less than 1.5 is regarded to as the quasi-linear solution. The shaded area is where the stable quasi-linear solution is not obtained, i.e., no steady solution is obtained, the obtained quasi-linear solution is unstable, or normalized form drag of the obtained stable solution is greater than 1.5. Three panels are different in the value of A_H . The value of A_H increase from the top to the bottom: $A_H = 1.0 \times 10^{-5} \pi^2$ in the top panel, $3.0 \times 10^{-5} \pi^2$ in the middle panel and $5.0 \times 10^{-5} \pi^2$ in the bottom panel. This figure shows that the critical U_N is around $|C_{23}|_N$ independent of η_0 and A_H .

Another feature seen in Fig. 3 is that the form drag of the stable quasi-linear solution becomes far larger than the linear one in the vicinity of $|C_{23}|_N$. This solution extends as a different solution from the quasi-linear solution for $U > |C_{23}|_N$. Therefore two solutions are found for $U > |C_{23}|_N$; the unstable quasi-linear one and the large form drag solution. While $B_{21} \cdot \eta_0 < 0$, i.e., the coefficient of $\sin 2x \sin y$ is opposite to the bottom topography in the former solution, $B_{21} \cdot \eta_0 > 0$ in the latter solution.

The (2, 1) mode is dominant and other modes are small in the quasi-linear solution, and therefore the quasi-linear solution is not affected by the low order truncation very much. In the large form drag solution, on the other hand, other modes than the (2, 1) mode are not small, and therefore it is thought to be affected by the low order truncation.

Here, we only note that it is implied that a large form drag solution exists for U_N where the quasi-linear solution is unstable. And the detail discussion on the solution whose form drag is far larger than that of the linear one will be in section 3.3 with the high-order model.

3.2.2 $(N, M) = (1, 7)$ case

In the case with $(N, M) = (1, 3)$, contained waves are substantially only two, $(2n, m) = (2, 1)$ and $(2, 3)$, and the critical velocity is the phase speed of the higher mode, the $(2, 3)$ mode. If there are more higher modes, the phase speeds of other higher modes are also expected to be the critical U_N . To confirm this, we calculate the steady solutions with $(N, M) = (1, 7)$.

Figure 5 shows contours of the form drag of the quasi-linear solution stable to even modes, the same figure as Fig. 4 except for $(N, M) = (1, 7)$. The value of A_H increase from the top to the bottom. The value of the normalized form drag of the stable solution is around unity except near the boundary between the shaded area and the unshaded area. Near the boundary contours are dense, which means that form drag increase abruptly there.

In Fig. 5, the features seen in the $(N, M) = (1, 3)$ case are also clearly seen, especially when A_H is small. The critical velocity decreases discretely as η_0 increases. When $A_H = 1.0 \times 10^{-5}\pi^2$, it is around 0.38 for $\eta_0 < 0.075$, 0.17 for $0.075 < \eta_0 < 0.15$, and 0.09 for $0.15 < \eta_0$. When $A_H = 3.0 \times 10^{-5}\pi^2$, it is around 0.38 for $\eta_0 < 0.125$, 0.17 for $0.125 < \eta_0 < 0.3$, and 0.09 for $0.3 < \eta_0$. When $A_H = 5.0 \times 10^{-5}$, it is around 0.38 for $\eta < 0.15$ and 0.17 for $0.15 < \eta_0 < 0.3$, and 0.09 for $0.5 < \eta_0$. The constant values, $U_N \approx 0.38, 0.17$ and 0.09 , correspond to $|C_{23}|$, $|C_{25}|$, and $|C_{27}|$, respectively. That is, the critical velocity moves to the phase speed of a higher mode discretely as η_0 increases.

The fact that the critical velocity is $|C_{27}|_N$ independent of η_0 for $\eta_0 > 1.5$ in the case of $A_H = 1.0 \times 10^{-5}\pi^2$ implies that the phase velocities of higher modes can be critical velocity if they are included in the model, which will be confirmed with the high-order

model in section 3.3.

As A_H increases, especially for larger η_0 , this feature becomes less clear. In the case of $A_H = 5.0 \times 10^{-5}\pi^2$, the transition of the critical velocity is less discretely, especially for $\eta_0 > 0.3$. The relation between the critical velocity and a phase speed of a wave is unclear.

There is another effect of the increase of A_H . As A_H increases, the critical velocity moves to the phase speed of a lower mode for the same η_0 . For example, when $\eta_0 = 0.2$, the critical velocity is $|C_{27}|_N$ only when $A_H = 1.0 \times 10^{-5}\pi^2$ and it is around $|C_{25}|_N$ when $A_H = 3.0 \times 10^{-5}\pi^2$ or $5.0 \times 10^{-5}\pi^2$. It is due to that the higher modes are damped more effectively as A_H increase.

As we anticipate, the phase speeds of higher modes can be critical velocity if the mode is included in the model. As the amplitude of the bottom topography becomes larger, the critical velocity moves to the phase speed of a higher mode.

3.2.3 Resonance of a higher mode

It has been shown that the phase speed of a mode whose wave number is higher than the bottom topography is of great importance. Form drag is much larger than that of the linear solution there. It is thought to be due to the resonance of that mode. Here we show its possibility in the linear theory in the simplest case, $(N, M) = (1, 3)$.

The truncated vorticity equations in the case of $(N, M) = (1, 3)$ can be written as

$$\frac{dA_{21}}{dt} = \frac{2}{5}(\beta - 5U)B_{21} - \frac{2}{5}B_{21}Z_2 + \frac{18}{5}B_{23}Z_2 + \frac{2}{5}\eta_0Z_2 + \frac{2}{5}\eta_0U - 5A_H A_{21}, \quad (3.5)$$

$$\frac{dB_{21}}{dt} = -\frac{2}{5}(\beta - 5U)A_{21} + \frac{2}{5}A_{21}Z_2 - \frac{18}{5}A_{23}Z_2 - 5A_H B_{21}, \quad (3.6)$$

$$\frac{dZ_2}{dt} = (2B_{21} + \frac{1}{4}\eta_0)A_{23} - (2B_{23} + \frac{1}{4}\eta_0)A_{21} - 4A_H Z_2, \quad (3.7)$$

$$\frac{dA_{23}}{dt} = \frac{2}{13}(\beta - 13U)B_{23} + \frac{2}{13}(B_{21} - \eta_0)Z_2 - 13A_H A_{23}, \quad (3.8)$$

$$\frac{dB_{23}}{dt} = -\frac{2}{13}(\beta - 13U)A_{23} - \frac{2}{13}A_{21}Z_2 - 13A_H B_{23}. \quad (3.9)$$

Since the steady solution is considered, we neglect the left hand sides of these equations,

and take U as the control parameter of the system.

To make the problem linearly tractable we assume that the amplitude of the bottom topography and the diffusion coefficient are small:

$$\eta_0 = O(\varepsilon) = \varepsilon h, \quad A_H = O(\varepsilon) = \varepsilon \nu,$$

where ε is a small parameter. Using ε , we expand the dependent variables in the manner of

$$B_{21} = \sum_{j=0}^{\infty} \varepsilon^j B_{21}^{(j)}. \quad (3.10)$$

Since the forcing term to this equation set, $\frac{2}{5}\eta_0 U$, is of order ε , all the dependent variables are equal to or less than $O(\varepsilon)$, except when $\beta - 5U = O(\varepsilon)$. Our aim in this section is to show the possibility of the resonance of the (2, 3) mode, and therefore the situation where $\beta - 5U = O(\varepsilon)$ is not treated. Since $\frac{2}{5}(\beta - 5U)B_{21}$ and $\frac{2}{5}\eta_0 U$ must be balanced in the first order of (3.5),

$$B_{21}^{(1)} = -\frac{hU}{\beta - 5U}. \quad (3.11)$$

Then the lowest order of (3.6) is $O(\varepsilon^2)$, and therefore $A_{21} = \varepsilon^2 A_{21}^{(2)} + O(\varepsilon^3)$. Since $-\frac{2}{5}(\beta - 5U)A_{21}$ and $-5A_H B_{21}$ must be balanced,

$$A_{21}^{(2)} = \frac{5^2 \cdot h\nu U}{2 \cdot (\beta - 5U)^2}. \quad (3.12)$$

It should be noted here that the viscosity is indispensable for non-zero A_{21} to exist.

The term of $-\frac{1}{4}\eta_0 A_{21}$ in (3.7) acts as a forcing term to the equation set of (3.7)–(3.9), the lowest order of (3.7) is $O(\varepsilon^3)$. Therefore $A_{23} \leq O(\varepsilon^2)$, $B_{23} \leq O(\varepsilon)$, and $Z_2 \leq O(\varepsilon^2)$.

When $\beta - 13U = O(1)$, the magnitude of B_{23} must be equal to or less than $O(\varepsilon^3)$ since other terms than $\frac{2}{13}(\beta - 13U)B_{23}$ in (3.8) are equal to or less than $O(\varepsilon^3)$. And then the magnitude of A_{23} must be equal to or less than $O(\varepsilon^4)$ in the same way from (3.9). The other terms than $-\frac{1}{4}\eta_0 A_{21}$ and $-4A_H Z_2$ are less than $O(\varepsilon^3)$ in (3.7). Therefore $-\frac{1}{4}\eta_0 A_{21}$

and $-4A_H Z_2$ must be balanced, and

$$Z_2^{(2)} = -\frac{5^2 \cdot h^2 U}{2^5 (\beta - 5U)^2}. \quad (3.13)$$

It is interesting that for Z_2 to have this form, the viscosity is important, but Z_2 itself does not depend on the viscosity. Using this Z_2 , from (3.8) and (3.9) the leading terms of A_{23} and B_{23} , i.e., $A_{23}^{(4)}$ and $B_{23}^{(3)}$, can be written as,

$$A_{23}^{(4)} = \frac{5^2 \cdot h^3 U \nu \{5^2 \cdot U(\beta - 13U) + 13^2(\beta - 4U)(\beta - 5U)\}}{2^6 \cdot (\beta - 5U)^4 (\beta - 13U)^2}, \quad (3.14)$$

$$B_{23}^{(3)} = -\frac{5^2 \cdot (\beta - 4U) h^3 U}{2^5 \cdot (\beta - 13U)(\beta - 5U)^3}. \quad (3.15)$$

These equations imply that $A_{23}^{(4)}$ and $B_{23}^{(3)}$ become infinitely large as $U \rightarrow \frac{\beta}{13}$ and the expansions above break down. That is, the resonance occurs at $U = |C_{23}| (= \beta/13)$.

When $\beta - 13U = O(\varepsilon)$, equations (3.14) and (3.15) imply that A_{23} and B_{23} are of $O(\varepsilon^2)$. Since Z_2 is unchanged in this case, equations for A_{23} and B_{23} can be obtained as

$$-uB_{23}^{(2)} - 13\nu A_{23}^{(2)} = -\frac{3^2 \cdot 5^2}{2^{13} \beta} h^3, \quad (3.16)$$

$$uA_{23}^{(2)} - 13\nu B_{23}^{(2)} = 0, \quad (3.17)$$

where $u = \varepsilon^{-1} \frac{2}{13} (13U - \beta)$.

This set of equations is the same as that for a forced oscillator with a damping term. In this equation, the forcing term is the term on the right-hand side in (3.16). The solution becomes,

$$A_{23}^{(2)} = \frac{3^2 \cdot 5^2 \cdot 13 \cdot h^3 \nu}{2^{13} \cdot \beta (13\nu^2 + u^2)}, \quad (3.18)$$

$$B_{23}^{(2)} = \frac{3^2 \cdot 5^2 \cdot h^3 u}{2^{13} \cdot \beta (13\nu^2 + u^2)}. \quad (3.19)$$

The above solution suggests that the viscosity can excite the higher modes through the nonlinear term and can cause a higher mode wave resonance. In the numerical solutions discussed in the present study, A_H is small but η_0 is not. If we assume $A_H = O(\varepsilon)$ while

$\eta_0 = O(1)$, (3.18) and (3.19) suggest that A_{23} and B_{23} are of $O(\varepsilon^{-1})$ around $|C_{23}| - U = O(\varepsilon)$. Although such a situation cannot be treated by this linear theory, it can be expected that A_{21} and B_{21} will strongly be affected by the resonance. So, we may call the phase speed of the higher modes, $|C_{23}|$, the resonant velocity. It is thought that this kind of resonance could occur on higher modes in the higher order models and that the form drag swerves from the linear one around the resonant velocities of those modes.

3.2.4 Summary

In this subsection, the steady solution, mainly the quasi-linear solution, is studied in the low-order models. An interesting feature is found, that is, there exists a critical velocity beyond which the stable quasi-linear solution is not obtained. The critical velocity is not the phase speed of the $(2, 1)$ mode which is the same mode as the bottom topography, but the phase speed of higher modes. Around the critical velocity, the form drag is much larger than that of the linear solution. The critical velocity moves to the phase speed of a higher mode as η_0 increases.

The possibility that the resonance of a higher mode occur is shown in a linear theory. When U_N approaches a phase velocity of a higher mode, the coefficient of that mode can become large, which could be expected to affect the form drag.

The diffusion has mainly two effects. Firstly, as A_H increases, the coincidence of the critical velocity with the resonant velocity is unclear, which occurs especially when η_0 is large. Secondly, as A_H increases, the critical velocity apt to move to the phase speed of a lower mode when η_0 is same. It is because the higher modes are damped when A_H is large. And therefore the resonance of the mode is not thought to occur.

The quasi-linear solution is unstable for U_N larger than the critical velocity. It is shown that there exists a stable solution which gives large form drag and whose coefficient of $\sin 2x \sin y$ is same sign as the bottom topography. Since not only the $(2, 1)$ mode but also other modes are not small in the solution whose form drag is large, this solution is thought to be affected by the low order truncation. Therefore details of the solution is

not discussed in this subsection.

3.3 High-order Models

In the previous subsection we study steady solutions of the low-order models. Mainly the focus is on the quasi-linear solution, and find that the critical velocity exists beyond which the stable quasi-linear solution is not found.

In this subsection we show steady solutions of the high-order model calculated by the LMM. First, the quasi-linear solution is investigated by using the inviscid exact solution as the initial guess. Next, other steady solutions than the quasi-linear one are sought. It is expected that a solution whose form drag is larger than that of the linear one exist as in the low-order model of $(N, M) = (1, 3)$ in Fig. 3. These calculations are carried out mainly for $0 < U_N < 0.6$. It is because the maximum U_N for which the stable quasi-linear solution is obtained in the low-order models is around $|C_{23}|_N (\approx 0.38)$ in even the smallest η_0 case adopted here, and is smaller in the larger η_0 case, so that we anticipate that no stable quasi-linear solution is obtained for $U_N > 0.6$ in the high-order model, either.

We mean the high-order model as the fully nonlinear model in which the sufficiently large truncation numbers, (N, M) , is used for accurate computations. The sufficient truncation number depends on parameters in this system. The interaction term between the zonal mean velocity and the bottom topography, $U \frac{\partial \eta}{\partial x}$, acts as the forcing term in the potential vorticity equation (2.2). Therefore as the amplitude of the topography becomes larger, the truncation number which is necessary for accuracy increases. The truncation number, (N, M) , we use is $(10, 20)$ for cases of $\eta_0 \leq 0.1$, $(20, 40)$ for $\eta_0 \leq 0.5$ and $(25, 50)$ for $\eta_0 \leq 1.0$. We use, however, $(N, M) = (10, 20)$ independent of η_0 in the calculation of the quasi-linear solution (Fig. 6), for higher modes are small in the quasi-linear solution. The sufficiency of these truncation numbers were checked by comparing the results with those with larger truncation numbers.

Figure 6 shows form drag calculated from steady solutions obtained by the LMM. The

initial guess is the inviscid exact solution (3.2). The form drag is normalized by that of the linear solution, that is, the normalized form drag is $A_{21}/A_{21}^{(L)}$. The stable solution is denoted by solid lines, and the solution stable to even modes but unstable to odd modes is denoted by broken lines. Solutions unstable to even modes are not shown.

It is found that the phase speed of a wave whose wavenumber is higher than that of the bottom topography is the critical velocity also in the high-order model. Form drag swerves from the linear one and increases abruptly around a phase speed. As A_H increase, the U_N at which the normalized form drag begins to increase from unity goes away from the phase speed of a wave to a little smaller side. In the case of $A_H = 1.0 \times 10^{-5}\pi^2$, the normalized form drag swerves abruptly in the very vicinity of the phase speed. When $A_H = 3.0 \times 10^{-5}\pi^2$ and $5.0 \times 10^{-5}\pi^2$, the normalized form drag begins to increase less abruptly at a little smaller U_N than just the phase speed.

In the case of $A_H = 3.0 \times 10^{-5}\pi^2$, the solution is stable to even modes but unstable to odd modes for $U_N > 0.28$ when $\eta_0 = 0.1$. The detail of this point will be shown in Fig. 17 and discussed later.

The feature that the critical velocity coincides with a phase speed of a wave and that it moves to phase speeds of higher modes with increase of η_0 can be seen more clearly in Fig. 7. Figure 7 is contours of normalized form drag in the $U_N-\eta_0$ plane, the same figure as Fig. 4 and Fig. 5. Figures 5 and 7 are very similar. It is inferred that resonance of the higher mode can occur similar to the resonance discussed in section 3.2.3. The equation set for higher modes can be written in a similar form to (3.16) and (3.17) as well.

The notable difference in Figs. 5 and 7 is that $|C_{29}|_N$ is also the critical velocity for $\eta_0 > 0.5$ in the case of $A_H = 1.0 \times 10^{-5}\pi^2$ as is expected in section 3.2.2. Besides, the relation between the critical velocity and a phase speed is a little less clear in the high-order model than in the low-order model. As seen in the $(N, M) = (1, 7)$ case, the relation become less clear as A_H increase. Therefore it is thought that nonlinear terms relating to higher modes acts as a kind of dissipation. Though such differences exist, the

features seen in the low-order models are also seen in the high-order model. We consider it important to emphasize again that the critical velocity becomes smaller not gradually but discretely; namely the critical velocity is around a resonant velocity of a wave which is higher mode than that of the bottom topography in the high-order model.

These results mean that the quasi-linear solution exists only for very small U_N . This implies that the linear approximation is valid only for very small U_N ; even in the case of small η_0 the linear approximation is valid only for U_N smaller than $|C_{23}|_N$, if A_H is small.

When we use the inviscid exact solution as the initial guess, the LMM would not find any stable solution for larger U_N than the critical velocity. Only an unstable solution is found or any steady solution is not found. As mentioned in section 3.2, this does not necessarily mean that there is no stable solution, and the large form drag solution is expected to exist.

Here, we search a stable solution for $U_N > |C_{23}|_N$ by numerically integrating (2.2) with fixed U_N , using the unstable solution obtained by the LMM as the initial condition (the solution labeled 'A' in Fig. 9) in the case of $(\eta_0, A_H) = (0.1, 5.0 \times 10^{-5} \pi^2)$. Figure 8 shows the time series of the coefficients of the (2, 1) and the (2, 2) modes, i.e., A_{21} , B_{21} , A_{22} and B_{22} , where the (2, 1) mode is an even mode and the (2, 2) mode is an odd mode. As the initial state labeled 'A' in Fig. 9 consists of only even modes, A_{22} and B_{22} are zero initially. Since the initial condition is a steady solution unstable to even modes, A_{21} and B_{21} change rapidly, and at $t \approx 6000$ the time-dependent solution converges into another steady solution ('B' in Fig. 9), which also consists of only even modes (the coefficients of (2,2) remain 0). This steady solution is stable to even modes but unstable to odd modes. Therefore odd modes continue to grow and around $t \simeq 70000$ the effect of odd modes makes the transition to another steady solution ('C' in Fig. 9), which consists of both even and odd modes. This solution is stable to both even and odd modes, so no transition occur from that time on.

With these two steady solutions, one is stable and consists of both even and odd

modes and the other is unstable to odd modes, being initial guesses, two branches of steady solutions are obtained by the LMM (Fig. 9).

The branch unstable to odd modes (\triangle in Fig. 9) including the solution 'B' consists of only even modes, and the stable branch (\circ) including the solution 'C' consists of both even and odd modes. The latter branch is apparently one branch, but actually two branches whose even modes are same and odd modes are reverse sign each other are overlapped. For this system has a symmetry with respect to the odd modes.

As U_N becomes smaller, these three (apparently two) branches merge at a point where U_N is about 0.4 in the case of Fig. 9, and become a single stable branch consisting of only even modes for U_N smaller than the bifurcation point, which is a pitchfork bifurcation. The single stable branch vanishes at $U_N \approx 0.3$, a little smaller than that of the bifurcation point. On the other hand, the stable quasi-linear branch exists for $U_N \lesssim 0.37$. Therefore two stable steady solutions coexist for a fixed U_N in $0.3 \lesssim U_N \lesssim 0.37$. These two stable solutions are connected by an unstable branch.

It should also be noted that the resonant velocity of the bottom topography, $U_N = 1.0$, has no effect on the solution characteristics.

Results in cases of other values of A_H and η_0 are shown in Fig. 10, including the case shown in Fig. 9. The solutions are plotted for $0 \leq U_N \leq 0.6$ in this figure since no drastic change in the solution would occur for $U_N > 0.6$ as is implied in Fig. 9.

Any case in Fig. 10 has three (in fact four) branches: one small form drag branch (the quasi-linear branch) and two (in fact three) large form drag branches one of which is unstable to odd modes.

We can see the abrupt change of the form drag around the critical velocity, though the change in the case of $\eta_0 = 1.0$ is less abrupt. The form drag increases more sharply and more abruptly around the critical velocity as A_H decrease with the same η_0 (in the same row in Fig. 10) and η_0 decrease with the same A_H (in the same column in Fig. 10).

Chapter 4

Numerical experiments

In this chapter we show the results of numerical experiments in which the initially quiescent fluid is accelerated by the constant wind stress, τ . In the last chapter steady solutions have been discussed with U_N fixed. At a steady state the form drag balances with the wind stress as in (2.8). Therefore when the experiments are carried out, it might be anticipated that the steady solutions discussed in the previous chapter is realized. However, the following uncertainties remain.

- (i) The stable solution with U_N fixed is not necessarily stable when U_N is permitted to vary.
- (ii) When U_N is accelerated from the rest, there is no guarantees that the acceleration of U_N stops at the steady solution obtained in the last chapter, even if the steady solution is stable.
- (iii) What will happen, if no stable steady solution corresponding to imposed τ exist? For example, there is no stable steady solution between $5.0 \times 10^{-5} < \tau < 1.6 \times 10^{-4}$ in Fig. 9.

With regard to item (i), the stable solution when U_N is not permitted to vary is unstable when U_N is permitted to vary at least if it is unstable to the form drag instability (see section 2.3). Therefore of the stable solutions obtained by the LMM (Fig. 10), at least the asymmetric solutions which exists through a pitchfork bifurcation is unstable when

U_N is permitted to vary. For the form drag of that solution becomes small as U_N increase. If a plus perturbation is added to U_N in that solution, the solution is accelerated. Since no stable solution is not found for larger U_N in Fig. 10, U_N increases infinitely and no steady solution will be attained. If a minus perturbation is added to U_N , U_N decreases. If there is a steady solution for the smaller side of U_N which is stable when U_N is permitted to vary, the solution will land up this steady solution. If a stable steady solution is not found, the problem comes to item **(ii)**. In the case shown in Fig. 9, we confirmed these expectations, applying the wind stress $\tau = 1.7 \times 10^{-5}$ to the solutions labeled 'D' (Fig. 11) and 'C' (Fig. 12). When the initial condition is the solution 'D' in Fig. 9, which is the steady solution for a little smaller side of U_N than the steady solution corresponding to $\tau = 1.7 \times 10^{-5}$, U_N decreases and converges into the stable steady solution at $U_N \approx 0.31$. The form drag component A_{21} (the solid line in the middle panel in Fig. 11) changes a little. Since the steady solution the time-dependent solution converges into consists of only even modes, the coefficients of both the cosine and the sine component of the (2, 2) mode (the lowest panel) become 0. When the initial condition is the solution 'C', which is the solution for a little larger side of U_N , the acceleration does not stop, as shown in Fig. 12.

Of course, the difference in the stability characteristics between a constant U_N case and a varying U_N case can results from other factors than the form drag instability.

With regard to item **(ii)**, the solutions of the experiments are not necessarily attracted by the stable steady solutions obtained in the last chapter since we do not obtain all steady solutions of this system and since linearly stable solutions are not always nonlinearly stable.

The numerical experiments are carried out for the eight cases shown in Fig. 10. The results of the numerical experiments is classified into two. The first is the case that any time-dependent solutions converges and no oscillatory solution is obtained ($\eta_0 \geq 0.3$). The second is the case that oscillatory solutions are also obtained ($\eta_0 = 0.1$). This classification

seem to results mainly from the steady solutions discussed in the last chapter. When the quasi-linear solution and the large form drag solution are connected by a stable solution, it is the first case. When the two solutions are not connected by a stable solution, it is the second case. In all cases when the imposed τ is small enough for the stable quasi-linear solution to exist corresponding to it, the trajectory is attracted by it. Therefore the zonal mean velocity increases with the increase of the wind stress in this small τ cases. And the acceleration does not stop when the imposed τ is too large. This case is discussed later.

First, we show the results of the former case that no oscillatory solution is obtained. In this case, the wind-driven solution converges into the steady solution obtained by the LMM in the last chapter. Figure 13 is the example of that case. The upper panel of Fig. 13 is the case of $(\eta_0, A_H) = (0.5, 3.0 \times 10^{-5} \pi^2)$ and the lower is of $(\eta_0, A_H) = (0.5, 5.0 \times 10^{-5} \pi^2)$. In Fig. 13, the final value of U_N in the experiment is denoted by the asterisks, $*$. The symbols \bigcirc and \triangle denote steady solutions obtained by the LMM in the last chapter: \bigcirc denotes a stable solution and \triangle denotes a solution unstable to odd modes.

These results imply that the zonal mean velocity of this system in the steady state is mainly determined by η_0 and A_H , rather than by τ . The zonal mean velocity becomes almost constant or within a relatively narrow range near a resonant velocity for a wide range of the wind stress since the form drag (equal to τ in the steady state) increase sharply around a resonant velocity in Fig. 10. That is, when the strength of the wind stress changes, the zonal mean velocity does not change very much. When η_0 and/or A_H is large, the form drag increase less sharply around the resonant velocity as stated the last chapter. So the range of U_N is not so narrow in the $\eta_0 = 1.0$ case. But even the case of $\eta_0 = 1.0$, U_N becomes only about double if τ is made three or four times larger. At least when η_0 is small, the range is narrow.

Second, we show the results of cases of $\eta_0 = 0.1$ (Fig. 14). In these cases, oscillatory solutions are also obtained. In Fig. 14, the maximum and minimum values of the wind-driven solution are denoted by a pair of large dots, \bullet , when the solution does not converge. The stability of the quasi-linear solution differs between two panels in Fig. 14.

The lower panel shows the case of $(\eta_0, A_H) = (0.1, 5.0 \times 10^{-5} \pi^2)$, the same case as in Fig. 9. In this case no stable solutions are found for $5.0 \times 10^{-5} < \tau < 1.6 \times 10^{-4}$ as the asymmetric solution is unstable to the form drag instability. Not only when the forcing, τ , is in this range but also when $\tau = 3.0 \times 10^{-5}$ and $\tau = 4.0 \times 10^{-5}$, a steady state is not reached, though a stable solution with a fixed U_N exists. We confirmed that these steady solutions are unstable when U_N is permitted to vary, by the linear stability analysis. Another interesting point is the difference in the amplitude between the oscillations for $\tau > 8.0 \times 10^{-5}$ and $\tau < 8.0 \times 10^{-5}$. These difference seems to stem from the difference in the structure of solution. For $\tau < 8.0 \times 10^{-5}$, even modes dominate and odd modes does not grow. On the other hand, for $\tau > 8.0 \times 10^{-5}$, odd modes are significant as well as even modes. In the latter case, the oscillation where odd modes are very small occurs first and after the odd modes grow significantly, the amplitude changes. Figure 15 shows an example of the former case. The (2,2) mode, which is an odd mode, does not grow. Figure 16 shows an example of the latter case. For $t \lesssim 38000$, the odd modes, for example the (2,2) mode shown in the lowest panel, continues to grow but remains small. And around $t \approx 38000$ the odd modes grows large enough to change the solution. After then, the amplitude of U_N (the top panel) is smaller than before then, and both even modes and odd modes are significant.

The upper panel in Fig. 14 shows the case of $(\eta_0, A_H) = (0.1, 3.0 \times 10^{-5} \pi^2)$. In this case, a bifurcation occurs at $U_N \approx 0.27$ and the quasi-linear solution is unstable to odd modes for $U_N \gtrsim 0.27$. Figure 17 shows the details of this bifurcation. In Fig. 17, the linear stability is examined by treating U_N as a variable unlike the calculations in Fig. 9 and Fig. 10 where U_N is constant. The quasi-linear solution bifurcates into

three solutions; one unstable quasi-linear solution (symmetric solution) and two stable asymmetric solutions. The two asymmetric solutions overlap in Fig. 17 as in Fig. 9. When τ corresponding to this quasi-linear solution unstable to odd modes is imposed, i.e., $6.6 \times 10^{-6} < \tau < 2.0 \times 10^{-5}$, the trajectory is attracted by this unstable solution at first since this solution is stable to even modes. However, since this steady solution is unstable to odd modes, odd modes continue to grow and eventually the trajectory diverge away from it and is attracted by an asymmetric solution. The asymmetric solutions are destabilized for $\tau > 8.0 \times 10^{-6}$. Therefore, when $6.6 \times 10^{-6} < \tau < 8.0 \times 10^{-6}$, the asymmetric stable state is reached. When $8.0 \times 10^{-6} < \tau < 2.0 \times 10^{-5}$, on the other hand, the solution is quasi-periodic since the asymmetric solutions are unstable. An example of the latter oscillation is shown in Fig. 18. In this case, the solution approaches the steady state unstable to odd mode around $U_N \approx 0.34$ and stays for a while there before odd modes grow, and then the oscillation begins. When τ is large, the oscillation is more complex. Whether the oscillatory solution consists of only even modes or of both even modes and odd modes does not depend on τ in this case unlike the case of $(\eta_0, A_H) = (0.1, 5.0 \times 10^{-5} \pi^2)$. The oscillatory solution consists of only even modes only when $\tau = 5.0 \times 10^{-5}$ (Fig. 19). When $\tau > 5.0 \times 10^{-5}$ (the example of $\tau = 6.0 \times 10^{-5}$ is shown in Fig. 20) as well as when $\tau < 5.0 \times 10^{-5}$ (the example of $\tau = 4.0 \times 10^{-5}$ is shown in Fig. 21), the solution consists of both even and odd modes. In the case of $\tau = 4.0 \times 10^{-5}$ (Fig. 21), for $t \lesssim 190000$ odd modes are small and the solution is quasi-periodic consisting of only even modes, and around $t \approx 190000$ odd modes grow sufficiently and the oscillation manner changes drastically. In the case of $\tau = 6.0 \times 10^{-5}$ (Fig. 20), odd modes grow significantly by $t \lesssim 30000$ and the solution changes. The oscillation is, however, not (quasi) periodic both before and after odd modes grow significantly.

Thus, when the time-dependent solution does not converge, the behavior of the solution differs according to parameters; whether the solution consists of only even modes or of both even and odd modes, and whether the oscillation is (quasi) periodic or not. The

common feature is that the solution is not accelerated far over $|C_{23}|_N$, i.e., the oscillation starts soon after U_N exceeds $|C_{23}|_N$, and that the mean value of the maximum and the minimum U_N of the oscillatory solution is within a relatively narrow range.

When the imposed τ is too large, the acceleration does not stop, as easily expected. Such case can be classified into two. One is the case that no steady solutions corresponding to the given τ are not found; namely cases that τ is very large. In this case the acceleration continues without stopping. The other is the case that the obtained steady solution corresponding to the given τ is unstable to odd modes but stable to even modes. In this case the steady state stable to even modes but unstable to odd modes is realized first. However, odd modes continue to grow and finally the acceleration restarts. Figure 22 shows an example (the steady solution is referred to the upper panel in Fig. 13). Around $t \simeq 1000$, the acceleration stops. Since the U_N at $t \simeq 1000$ is somewhat larger than that of the steady solution, the deceleration occurs and the quasi-steady state is realized around $t \simeq 4 \times 10^3$. But since this state is unstable to odd modes, at around $t \simeq 11 \times 10^3$ the acceleration restarts after odd modes grow. There are some cases that the acceleration does not stop at a steady solution unstable to odd modes and that U_N continues to increase (for examples, $\tau \geq 1.35 \times 10^{-3}$ in the case of $(\eta_0, A_H) = (1.0, 3.0 \times 10^{-5}\pi^2)$ and $\tau \geq 2.2 \times 10^{-3}$ in the case of $(\eta_0, A_H) = (1.0, 5.0 \times 10^{-5}\pi^2)$). Although there is such a difference according to parameters, the acceleration does not stop after long time when the corresponding steady solution is unstable to odd modes. The oscillatory solution is not found in this case.

Figure 23 schematically summarizes the behavior of solutions. The stable quasi-linear solution exists for small τ . As τ increases, U_N of equilibrium in the experiments becomes large along the linear solution. When τ becomes larger than a certain magnitude depending on parameters such as A_H and η_0 , U_N (the mean value of the maximum and the minimum U_N in oscillatory cases) does not increase very much or decreases though τ increases. This occurs at a higher mode resonant velocity. When τ increases further,

the steady solution corresponding to it becomes unstable to odd modes and therefore the acceleration of U_N stops once in most cases but restarts after long time. When τ is too large for steady solutions to exist, the acceleration does not stop.

Figure 24 shows the streamlines (left) and the potential vorticity contours (right) of the steady states in the case of $(\eta_0, A_H) = (0.5, 3.0 \times 10^{-5})$. When $\tau = 3.0 \times 10^{-5}$ (panel (a)), the solution is the quasi-linear one. Both the potential vorticity contours and the streamlines are similar to the ambient potential vorticity contours (panel (c) in Fig. 25). The cyclonic (anticyclonic) circulation cell exists over the topographic elevation (depression). As τ increases, the circulation cell weakens (panel (b)), the circulation cell of opposite direction appears (panel (c)) and strengthens (panel (d)). The gradient of the potential vorticity over the topographic elevation and depression weakens as τ increases (right panels in Fig. 24). Although the wind stress τ in case (c) is twice as large as that in case (b), for example, the zonal mean velocity is almost same. The circulation cells are strengthened instead of the zonal mean velocity being accelerated.

This feature of the large form drag solution (panel (d)) is qualitatively independent of η_0 , i.e., independent of the existence of the closed ambient potential vorticity contours. The ambient potential vorticity distribution is shown in Fig. 25. In the case of $\eta_0 = 0.1$ the ambient potential vorticity is modified only a little and any contour does not close. In the case of $\eta_0 = 0.3$ any contour does not close either but near the limit of unclosing. In the case of $\eta_0 = 0.5$ some of them close. Figure 26 shows the streamlines (left) and the potential vorticity of the solution for near the uppermost τ with which the steady state is reached. The amplitude of the bottom topography, η_0 , increase from the top panel to the bottom panel. This figure shows the example of cases where any ambient potential contour does not close (Fig. 25). The circulation cells in the streamlines exist over the topographic elevation and the depression and their directions are same independent of η_0 . The size of the cells, however, become large with the increase of η_0 . And the gradient of the potential vorticity also becomes large. When $\eta_0 = 0.1$, it is homogenized well.

Chapter 5

Summary and Discussion

We have studied one of the most basic problems of the form drag in a simple situation, a barotropic quasi-geostrophic β plane channel with a sinusoidal bottom topography, motivated by the recent results and discussions about the form drag in the Antarctic Circumpolar Current. Our main concern is whether the acceleration can stop and, if it can, what value the zonal mean velocity, U_N , will result when the fluid at rest is accelerated by a wind stress in the system where the momentum sink is only the form drag.

Before performing numerical experiments in which U_N are permitted to vary, we investigate the steady state under the condition that U_N is fixed in Chapter 3. When U_N is smaller than a certain value, the stable quasi-linear solution exists. The quasi-linear solution was not obtained or was unstable for U_N larger than this U_N value, the critical U_N . Around the critical U_N , the form drag increase abruptly. Although the critical U_N depends on the amplitude of the bottom topography, η_0 , and the horizontal diffusion coefficient, A_H , it is around the phase speed of a wave whose wave number is higher than that of the bottom topography. We refer to this velocity as the resonant velocity of the wave since it is inferred that the resonance of the mode can occur from the linear theory in section 3.2.3. While there are infinite number of the resonant velocities corresponding to the wavenumber, which resonant velocity is chosen depends on η_0 and A_H . As the amplitude of the bottom topography, η_0 , which acts as the forcing term, increase, and as the coefficient of the horizontal diffusion, A_H , decrease, the critical velocity moves the res-

onant velocity of a higher mode. The diffusion obscures the relation between the resonant velocity and the critical U_N , and when η_0 is large the relation also becomes unclear.

Other three solutions than the quasi-linear one are found for larger U_N which are strongly nonlinear and give large form drag. Two of them are asymmetric solutions, whose even modes are same and odd modes are opposite each other. Their form drag is the same, and therefore they are overlapped in bifurcation diagrams whose vertical axis is form drag, such as in Fig. 9. They are stable when U_N is fixed, but unstable to the form drag instability when U_N is unfixed. The other is symmetric solution which is stable to even modes but unstable to odd modes. When η_0 and A_H is small, the stable quasi-linear solution and the stable large form drag solution coexist for a fixed U_N in some range of U_N and those solutions are connected by an unstable solution. Otherwise, the stable quasi-linear solution and the stable large form drag solution is connected by a stable solution. In any case, the form drag of the stable solution increases abruptly when the control parameter U_N becomes larger than a critical U_N near a resonant velocity.

Next, we carried out a series of numerical experiments in Chapter 4 where the spatially uniform surface stress τ is applied on the resting ocean. In the case that the stable steady solution corresponding to the given τ is obtained when U_N is fixed, the zonal flow is accelerated to this U_N and becomes steady in most cases, and otherwise oscillates. Since the form drag changes rapidly around the resonant velocity, the resulting zonal flow velocity achieved in the experiment is near the resonant velocity in a wide range of the surface wind stress τ . When an experiment with larger τ is performed, the U_N cannot land on any steady value but is accelerated infinitely. Although many papers (e.g., Rambaldi and Mo, 1984) suggested the importance of the resonant velocity to the $(2, 1)$ mode whose wavenumber is the same as that of the bottom topography, this velocity has no effect on the form drag, if the quasi-linear solution turns unstable at a higher mode resonant velocity. In the case that a stable steady solution was not obtained corresponding to the imposed τ , a steady state does not occur but an oscillatory state appears. Although

the manner of oscillation depends on parameters, the mean value of the maximum and the minimum U_N is within a narrow range. This implies that U_N of equilibrium, whether it is steady or oscillatory, is determined to a large extent by η_0 and A_H , not τ , except for large τ cases where the acceleration does not stop, and for small τ cases where U_N is determined by τ along the quasi-linear solution, and that it is near a resonant velocity in many cases.

This system has been used mainly in the study of the atmospheric phenomena such as blocking since Charney and DeVore (1979), especially in the 1980s. In the atmosphere, the Ekman friction is dominant and therefore it was used as a dissipation in those studies. In the present system, on the other hand, the bottom Ekman friction is ignored and the horizontal diffusion is used. It is because in the oceans the horizontal diffusion is thought to be more important as the dissipation at least in large scale motions. Additionally, it is because many recent studies support that the dominant sink of the zonal momentum in the ACC is the form drag rather than the bottom friction and therefore we study the case that the zonal momentum sink is only form drag.

At least in the low-order model, the resonance discussed in section 3.2.3 could occur if the Ekman friction were used since equations are almost the same. It is, however, questionable if the swerving of the form drag from the linear solution could occur around the higher mode resonant velocities in the high-order model when the Ekman friction is adopted. In the case of the horizontal diffusion as in the present study, the significance of the damping term strongly depends on the wavenumber of the mode. It implies that there is the relatively large difference between the damping effect on two neighboring modes. If we take U_N as the control parameter, when U_N is small, the damping effect on the resonant mode corresponding to the U_N is significant so that the solution remains similar to the linear one. As U_N increases, the damping effect decreases and the resonance can occur overcoming the damping effect. Therefore, the solution change occurs abruptly. For example, it is possible that the damping effect on the $(2, 2m + 3)$ mode is very large when

U_N is near $|C_{2, 2m+3}|_N$ but that the effect on the $(2, 2m + 1)$ mode is not so large that the resonance of the $(2, 2m + 1)$ mode can occur when U_N increase to near $|C_{2, 2m+1}|_N$. On the other hand, in the case of the Ekman friction, the difference between the damping effect on two neighboring modes are not so large. The situation that only one resonance affects the solution seems to be difficult to occur. It would be expected that U_N around which the swerving of the form drag occurs would decrease gradually, or in less clearly step-wise manner, as η_0 and/or the coefficient of the friction increase in the Ekman friction case. In contrast, the swerving U_N would decrease in more clearly step-wise manner if a higher order friction such as a biharmonic friction were used.

Although simulations become the main stream in theoretical and/or numerical study on the Antarctic Circumpolar Currents, their simple model studies have still carried out recently. Wang and Huang (1995) analytically solved the homogeneous channel model and showed that the form drag is large when all geostrophic contours are blocked by the channel wall. Völker (1999) showed that strong form drag is generated by the resonance of baroclinic Rossby waves. In contrast to these work, we focus our attention on strong nonlinearity. The notable result is that the form drag can be large around a resonant velocity of waves whose wave number is higher than that of the bottom topography. And therefore the zonal mean velocity in the equilibrium is around the resonant velocity in a wide range of the surface wind stress when the initially quiescent fluid is accelerated by the constant wind stress.

The present model is too simple to discuss the ACC quantitatively. An essential point for the quantitative discussion is role of baroclinicity. Olbers and Völker (1996) and Olbers (1998) demonstrated that even an analytically manageable simple model with baroclinicity yields reasonable transport magnitudes. In the barotropic model, the surface wind stress directly drives the bottom zonal velocity. In the baroclinic model, on the other hand, the bottom zonal velocity is not directly driven by the surface wind stress. The surface wind drives uppermost layer and the zonal momentum is transferred by the

interfacial form drag (Olbers, 1998 ; Straub, 1993). Eddies are needed in the interfacial form drag, and it is thought that the eddies result from baroclinic instability. Therefore if eddies are not developed enough to transfer the momentum vertically, only the uppermost layer will be accelerated infinitely. In the real ocean, of course, the acceleration will stop. When the acceleration stops, it is interesting to study whether the resonant velocities of waves play the same role as in the present model. Another point that should be discussed further is the bottom topography. In the present study, we treat the case that the bottom topography consists of a single wave. Cases of other shapes of the bottom topography should be considered.

Acknowledgments

The GFD-DENNOU Library was used for producing the figures and for calculations of the fast Fourier transform.

Appendix

A. the linear stability analysis

We outline the linear stability analysis used in this study.

Assume that $\mathbf{X}_0 = (X_{01}, X_{02}, \dots, X_{0m})^T$ is the steady solution of equation

$$\frac{d\mathbf{X}}{dt} = \mathbf{f}(\mathbf{X}), \quad (\text{A.1})$$

where $\mathbf{X} = (X_1, X_2, \dots, X_m)^T$, $\mathbf{f}(\mathbf{X}) = (f_1(\mathbf{X}), f_2(\mathbf{X}), \dots, f_m(\mathbf{X}))^T$, i.e.,

$$\mathbf{f}(\mathbf{X}_0) = \mathbf{0}.$$

We consider the evolution of an infinitesimal perturbation, \mathbf{x}' , added to the steady solution. Substituting $\mathbf{X} = \mathbf{X}_0 + \mathbf{x}'$ into (A.1) gives the equation

$$\frac{d\mathbf{x}'}{dt} = \mathbf{f}(\mathbf{X}_0 + \mathbf{x}'). \quad (\text{A.2})$$

Since \mathbf{x}' is infinitesimal, the term on the right-hand side of (A.2) can be expanded as

$$\frac{d\mathbf{x}'}{dt} \approx \mathbf{J}_0 \mathbf{x}', \quad (\text{A.3})$$

where

$$\mathbf{J}_0 = \left[\begin{array}{ccc} \frac{\partial f_1}{\partial x_1} & \dots & \frac{\partial f_1}{\partial x_m} \\ \vdots & \ddots & \vdots \\ \frac{\partial f_m}{\partial x_1} & \dots & \frac{\partial f_m}{\partial x_m} \end{array} \right]_{\mathbf{X}=\mathbf{X}_0}. \quad (\text{A.4})$$

Therefore if all eigenvalues of the matrix \mathbf{J}_0 is less than 0, the solution \mathbf{X}_0 is stable.

Otherwise it is unstable. In this study, $m = (2 \times N + 1) \times M$ and

$\mathbf{X} = (A_{21}, A_{22}, \dots, A_{2NM}, B_{21}, B_{22}, \dots, B_{2NM}, Z_1, Z_2, \dots, Z_M)$, where A , B and Z is

defined in (2.5), and $f_1, f_2, \dots, f_{(2N+1)M}$ are the right-hand side of equations of $A_{21}, A_{22}, \dots, A_{2NM}, B_{21}, B_{22}, \dots, B_{2NM}, Z_1, Z_2, \dots, Z_M$, respectively.

When h is very small value,

$$\frac{\partial f_i}{\partial x_j} \approx \frac{f_i(X_{01}, X_{02}, \dots, X_{0j} + h, \dots, X_{0m}) - f_i(\mathbf{X}_0)}{h}. \quad (\text{A.5})$$

Therefore we numerically calculate the term on the right-hand side of (A.5) in the calculation of (A.4). The nonlinear terms, $J(\phi, \nabla^2 \phi)$, included in \mathbf{f} , is calculated at grid points in physical space, and then it is expanded to the orthogonal functions, which is the same as in the calculation of the steady solution with the LMM and in the numerical integrations.

B. the Levenberg-Marquardt-Morrison method

Steady solutions are calculated by the Levenberg-Marquardt-Morrison method (LMM) which is included in the Scientific Subroutine Library II. The outline of the LMM is as follows.

Define $F(\mathbf{x})$ as

$$F(\mathbf{x}) = \|\mathbf{f}(\mathbf{x})\|^2 = \sum_{i=1}^m \{f_i(x)\}^2,$$

where $\mathbf{f}(\mathbf{x}) = (f_1(\mathbf{x}), f_2(\mathbf{x}), \dots, f_m(\mathbf{x}))^T$ and $\mathbf{x} = (x_1, x_2, \dots, x_n)^T$. The LMM is a method which gives a minimum value, $F(\mathbf{x}^*)$, and \mathbf{x}^* . When a initial guess \mathbf{x}_k is given, the new vector \mathbf{x}_{k+1} is defined as $\mathbf{x}_{k+1} = \mathbf{x}_k + \Delta \mathbf{x}_k$ and it is iterated until a minimum value, $F(\mathbf{x}^*)$, is obtained. $\Delta \mathbf{x}_k$ is determined as satisfies the equation,

$$(\mathbf{J}_k^T \mathbf{J}_k + \nu_k^2 \mathbf{I}) \Delta \mathbf{x}_k = -\mathbf{J}_k^T \mathbf{f}(\mathbf{x}_k),$$

where \mathbf{J}_k is Jacobian: $\mathbf{J}_k = \begin{bmatrix} \frac{\partial f_1}{\partial x_1} & \dots & \frac{\partial f_1}{\partial x_n} \\ \vdots & \ddots & \vdots \\ \frac{\partial f_m}{\partial x_1} & \dots & \frac{\partial f_m}{\partial x_n} \end{bmatrix}$, and ν_k is a positive number called

Marquardt number, the value of which is determined every step of the iteration.

The direction of $\Delta \mathbf{x}_k$ is the same as that in the Newton-Gauss method when $\nu_k \rightarrow 0$, and is the same as that in the steepest descent method when $\nu_k \rightarrow \infty$. Therefore the LMM can calculate \mathbf{x}^* stably and with less iterations compensating for weak points in those two methods by determining the proper ν_k .

References

- Charney, J. and J. G. DeVore (1979): Multiple flow equilibria in the atmosphere and blocking. *J. Atmos. Sci.*, **36**, 1205-1216.
- Charney, J. and D. M. Straus (1980): Form-drag instability, multiple equilibria and propagating planetary waves in baroclinic, orographically forced, planetary wave systems. *J. Atmos. Sci.*, **37**, 1157-1176.
- FRAM Group (1991): An eddy-resolving model of the Southern Ocean. *Eos, Trans. Amer. Geophys. Union*, **72**, 169-175.
- Gille, S. T. (1997): The Southern Ocean momentum balance: evidence for topographic effects from numerical model output and altimeter data. *J. Phys. Oceanogr.*, **27**, 2219-2232.
- Gnanadesikan, A and R. W. Hallberg (2000): On the relationship of the Circumpolar Current to southern hemisphere winds in coarse-resolution ocean models. *J. Phys. Oceanogr.*, **30**, 2013-2034.
- Hidaka, K. and M. Tsuchiya (1953): On the antarctic circumpolar current. *J. Mar. Res.*, **12**, 214-222.
- Klinck, J. M. (1992): Effects of wind, density, and bathymetry on a one-layer Southern Ocean model. *J. Geophys. Res.*, **97**, 20179-20189.
- McWilliams, J. C. (1977): A note on a consistent quasi-geostrophic model in a multiply connected domain. *Dyn. Atmos. Oceans*, **1**, 427-441.
- McWilliams, J. C., W. R. Holland and J. H. S. Chow (1978): A description of numerical Antarctic Circumpolar Current. *Dyn. Atmos. Oceans*, **2**, 213-291

- Mukougawa, H. and I. Hirota (1986): Nonlinear evolution of forced Rossby waves in a barotropic atmosphere Part I: Stability properties of forced Rossby waves. *J. Meteor. Soc. Japan*, **64**, 197-211.
- Munk, W. H. (1950): On the wind-driven ocean circulation. *J. Meteorology*, **7**, 79-93
- Munk, W. H. and E. Palmén (1951): Note on the dynamics of the Antarctic Circumpolar Current. *Tellus*, **3**, 53-55.
- Olbers, D. and C. Völker (1996): Steady states and variability in oceanic zonal flow. p. 407-443. In *Decadal Climate Variability Dynamics and Predictability*, ed. by D. L. T. Anderson and J. Willebrand, Springer-Verlag.
- Olbers, D. (1998): Comments on “ On the obscurantist physics of “form drag” in theorizing about the Circumpolar Current.”. *J. Phys. Oceanogr.*, **28**, 1647-1654.
- Pedlosky, J. (1981): Resonant topographic waves in barotropic and baroclinic flows. *J. Atmos. Sci.*, **38**, 2626-2641.
- Rambaldi, S. and K. C. Mo (1984): Forced stationary solutions in a barotropic channel: multiple equilibria and theory of nonlinear resonance. *J. Atmos. Sci.*, **21**, 3135-3146.
- Speer, K., S. R. Rintoul and B. Sloyan (2000): The Diabatic Deacon Cell. *J. Phys. Oceanogr.*, **30**, 3212-3222.
- Stommel, H. (1948): The westward intensification of wind-driven ocean currents. *Trans. AGU*, **29**, 202-206
- Stommel, H. (1957): A survey of ocean current theory. *Deep-sea Res.*, **4**, 149-184.
- Straub, D. N. (1993): On the transport and angular momentum balance of channel models of the Antarctic Circumpolar Current. *J. Phys. Oceanogr.*, **23**, 776-782.
- Sverdrup, H. U. (1947): Wind-driven currents in a baroclinic ocean, with application to the equatorial currents of the eastern Pacific. *Proc. Nat. Acad. Sci.* , **33**, 318-326.
- Tansley, C. E. and D. P. Marshall (2001): On the dynamics of wind-driven Circumpolar Current. *J. Phys. Oceanogr.*, **31**, 3258-3273.

- Tian, Y., E. R. Weeks, K. Ide, J. S. Urbach, C. N. Baroud, M. Ghil and H. L. Swinney (2001): Experimental and numerical studies of an eastward jet over topography. *J. Fluid Mech.*, **438**, 129-157.
- Treguier, A. M. and J. C. McWilliams (1990): Topographic influences on wind-driven, stratified flow in a β -plane channel: an idealized model for the Antarctic Circumpolar Current. *J. Phys. Oceanogr.*, **20**, 321-343.
- Tung, K.K. and A. J. Rosenthal (1985): Theories of multiple equilibria, a critical reexamination. Part 1: Barotropic models. *J. Atmos. Sci.*, **42**, 2804-2819
- Tung, K.K. and A. J. Rosenthal (1986) : On the extended-range predictability of large-scale quasi-stationary patterns in the atmosphere, *Tellus*, **38A**, 333-365.
- Völker, C (1999): Momentum Balance in zonal flows and resonance of baroclinic Rossby waves. *J. Phys. Oceanogr.*, **29**, 1666-1681.
- Wang, L., and R. X. Huang (1995): A linear homogeneous model of wind-driven circulation in a β -plane channel. *J. Phys. Oceanogr.*, **25**, 587-603.
- Warren, B., J. LaCasce and P. A. Robbins (1996): On the obscurantist physics of “form drag” in theorizing about the Circumpolar Current. *J. Phys. Oceanogr.*, **26**, 2297-2301.
- Wolff, J. O., E. Maier-Reimer and D. J. Olbers (1991): Wind-driven flow over topography in a zonal β -plane Channel: a quasi-geostrophic model of the Antarctic Circumpolar Current. *J. Phys. Oceanogr.*, **21**, 236-264.
- Yoden, S. (1985): Multiple stable states of quasi-geostrophic barotropic flow over sinusoidal topography. *J. Meteor. Soc. Japan*, **63**, 1031-1045.

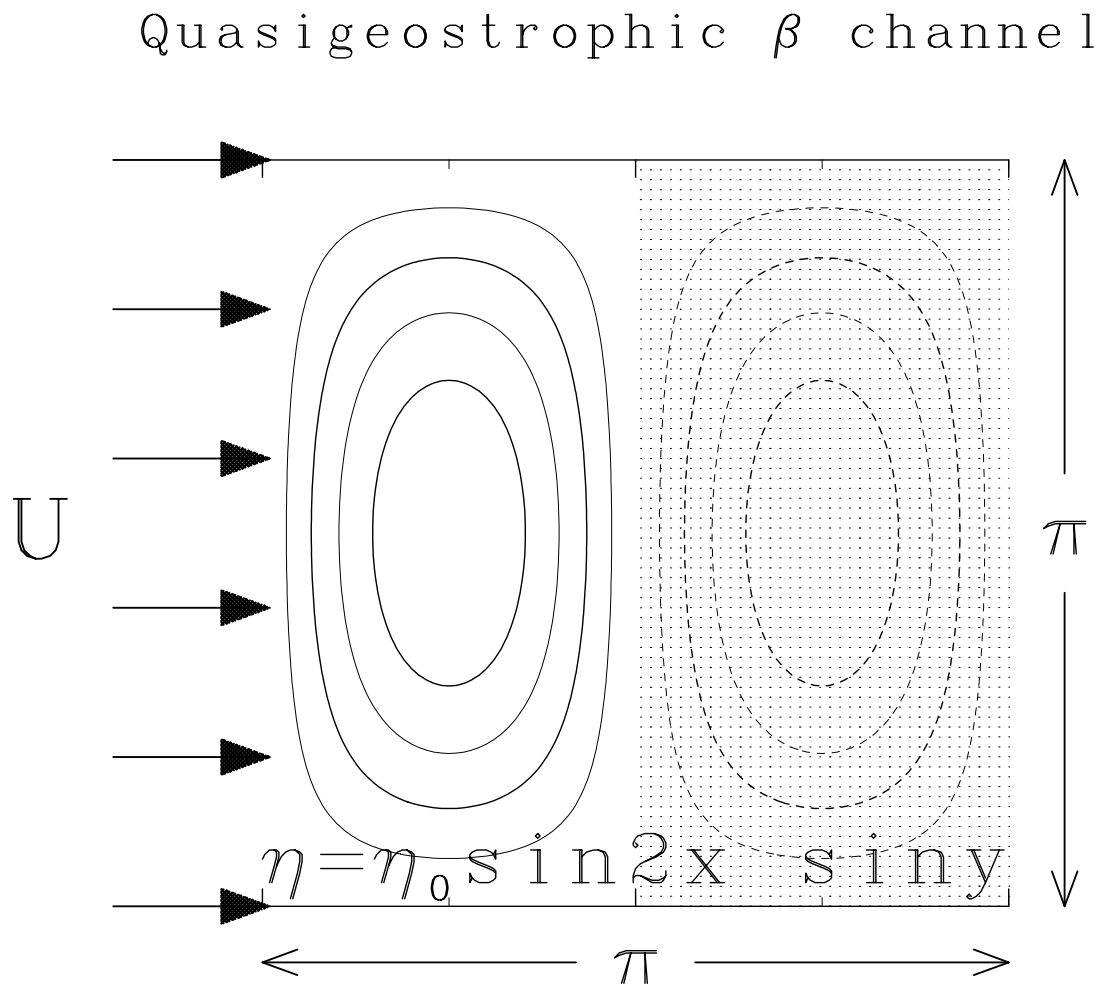


Figure 2: Model domain. Contours denote the bottom topography. Shaded region is the depression of the topography.

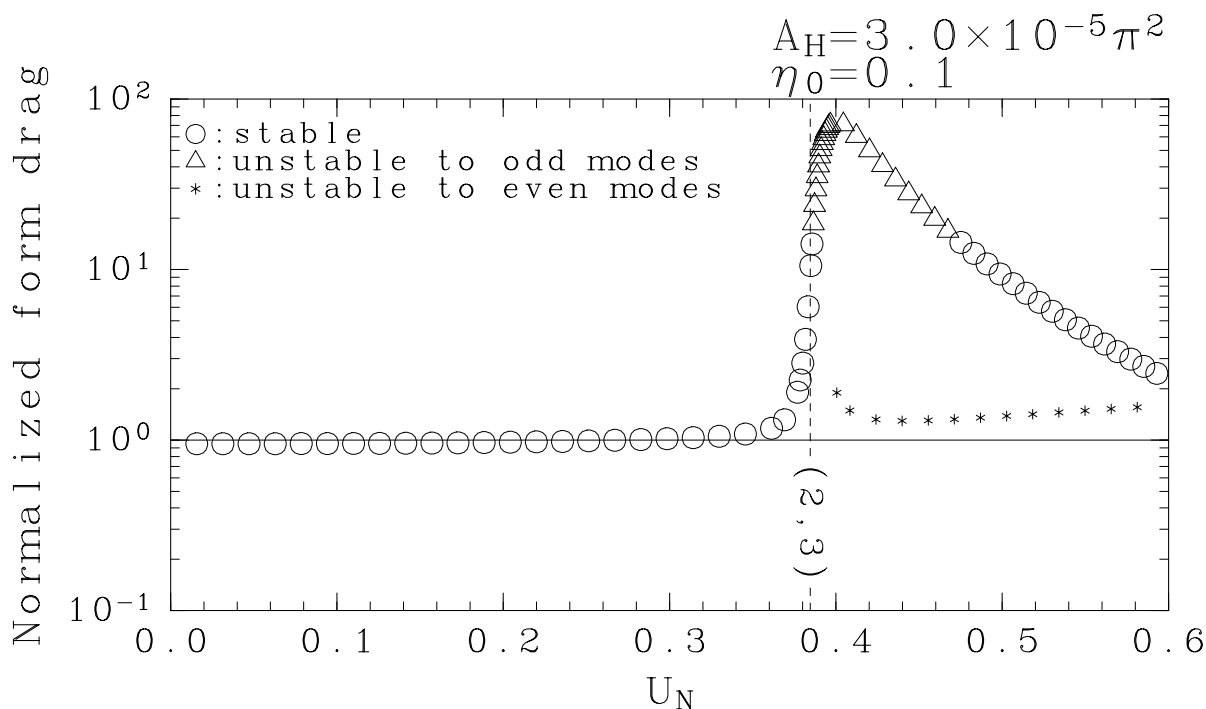


Figure 3: An example of form drag of the steady solution in the low-order model: $(N, M) = (1, 3)$. The magnitude of form drag is normalized by that of the linear solution. The vertical axis is a logarithmic coordinate. Stable solutions are plotted by \circ , solutions unstable to only odd modes by \triangle , and solutions unstable to even modes by $*$. The solid line denotes the linear solution. The vertical dotted line denotes $|C_{23}|$ (≈ 0.38). $\eta_0 = 0.1$, and $A_H = 3.0 \times 10^{-5} \pi^2$.

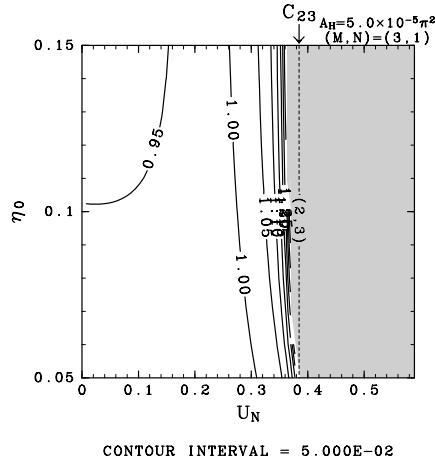
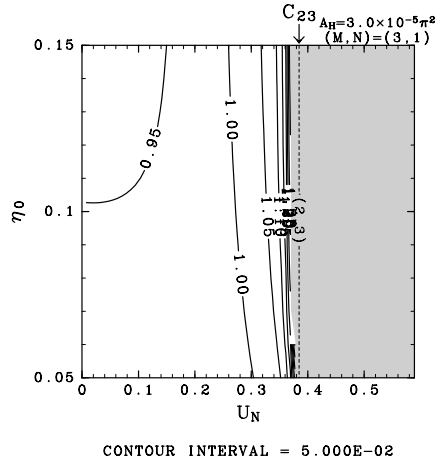
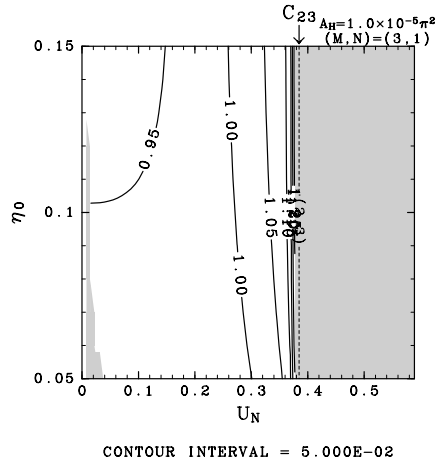
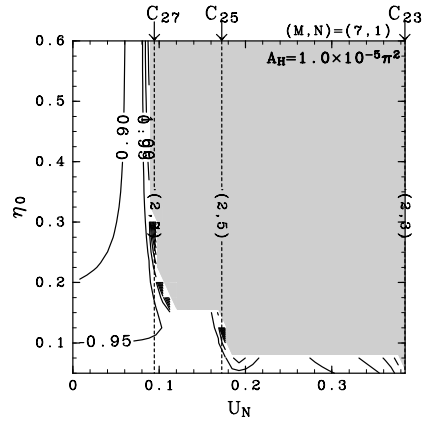
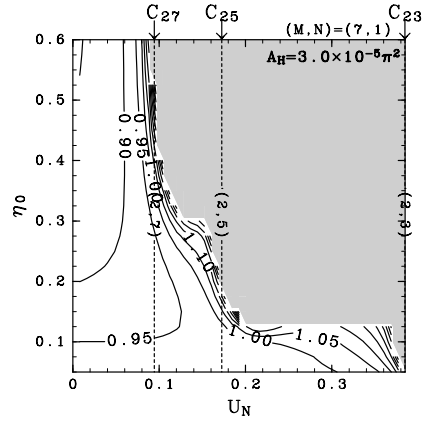


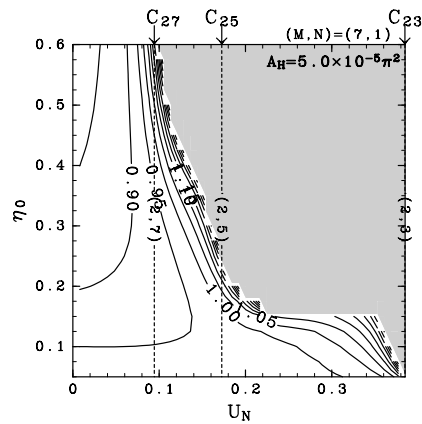
Figure 4: Contours of the form drag of the quasi-linear solution stable to even modes calculated with $(N, M) = (1, 3)$. The magnitude of the form drag is normalized by that of the linear solution. The shaded area is where the stable quasi-linear solution is not obtained. Contours larger than 1.5 are not drawn. $|C_{23}|_N$ is indicated by the arrow on the top of each panel and by the dotted line.



CONTOUR INTERVAL = 5.000E-02



CONTOUR INTERVAL = 5.000E-02



CONTOUR INTERVAL = 5.000E-02

Figure 5: Same as Fig. 4 but for $(N, M) = (1, 7)$. $|C_{23}|_N$, $|C_{25}|_N$ and $|C_{27}|_N$ are indicated by arrows on the top of each panel and by the dotted lines.

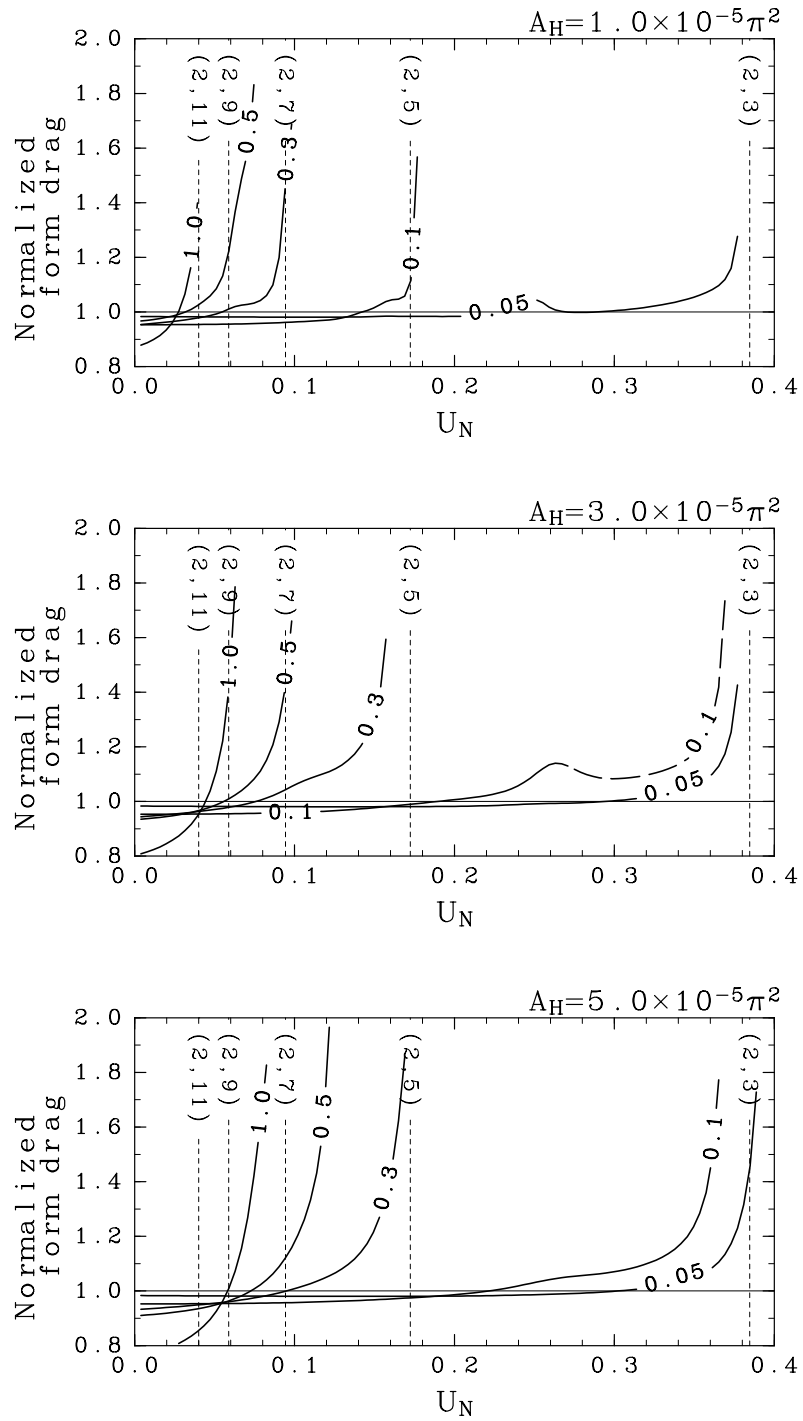


Figure 6: Form drag of solution in the high-order model obtained by the LMM. The magnitude of the form drag is normalized by the linear one. Numerical values on lines denote η_0 . A broken line denotes solutions unstable to odd modes but stable to even modes. Solutions unstable to even modes are not shown. Vertical dotted lines show resonant velocities corresponding to the wave number written on them.

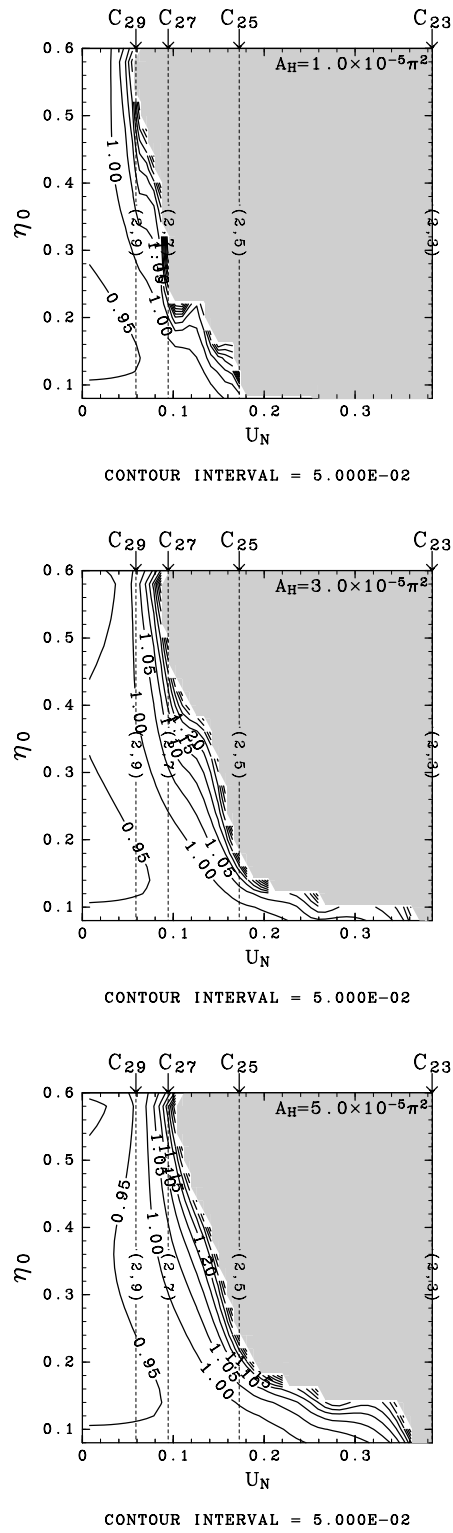


Figure 7: Same as Fig. 4 but for $(N, M) = (10, 20)$. $|C_{23}|_N$, $|C_{25}|_N$, $|C_{27}|_N$ and $|C_{29}|_N$ are indicated by arrows on the top of each panel and by the dotted lines.

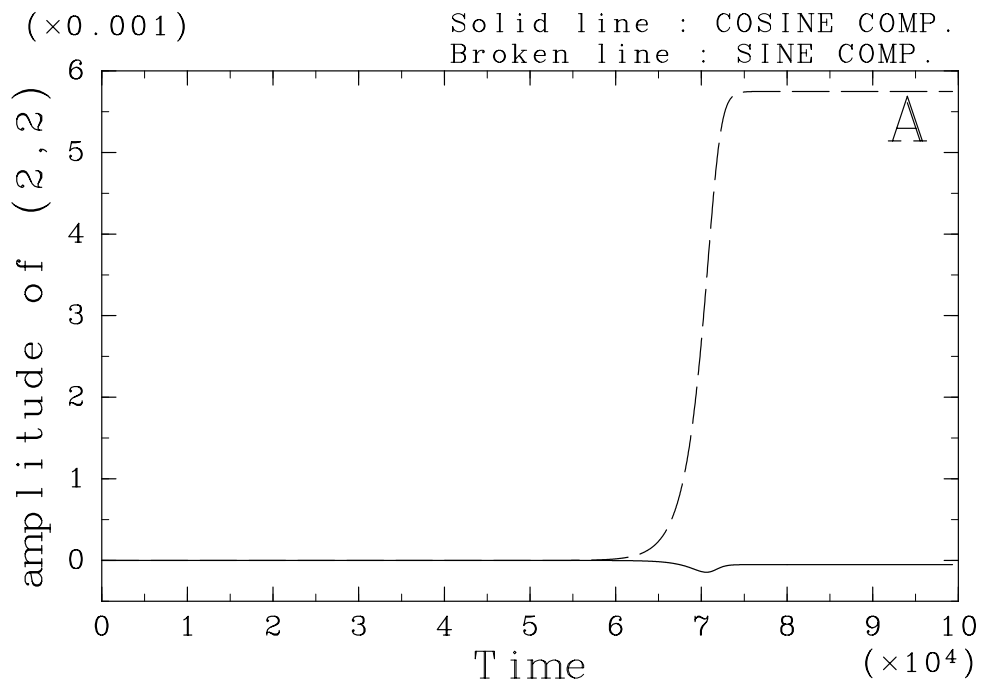
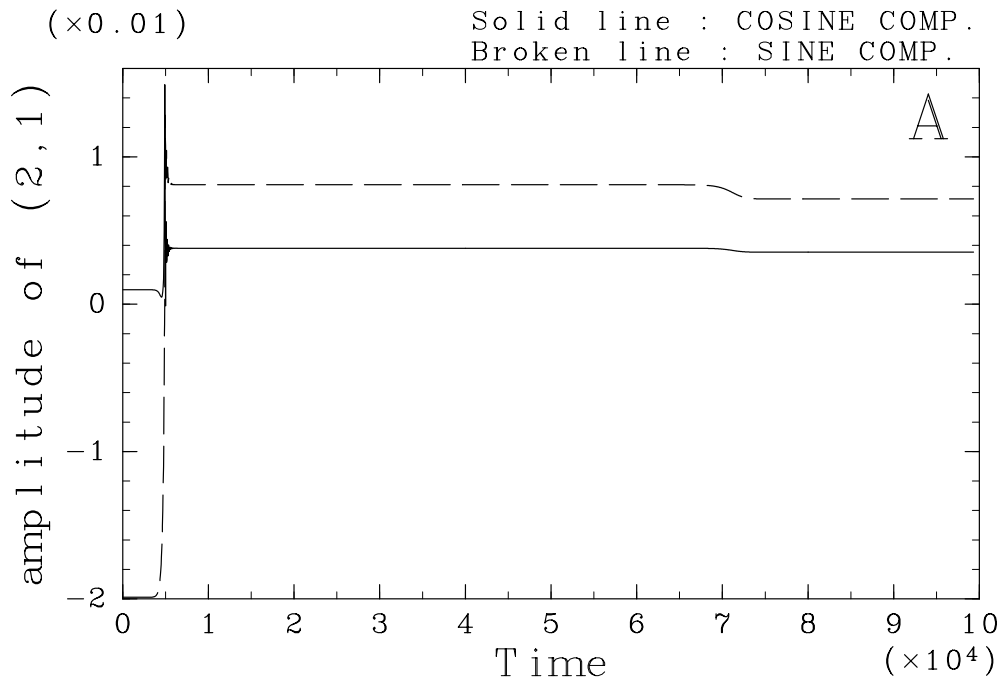


Figure 8: The time series of the coefficients of (2,1) (the upper panel) and (2,2) (the lower panel). The integration is started from the solution labeled 'A' in Fig. 9. The solid line is cosine component and the broken line is sine component. $(N, M) = (10, 20)$.

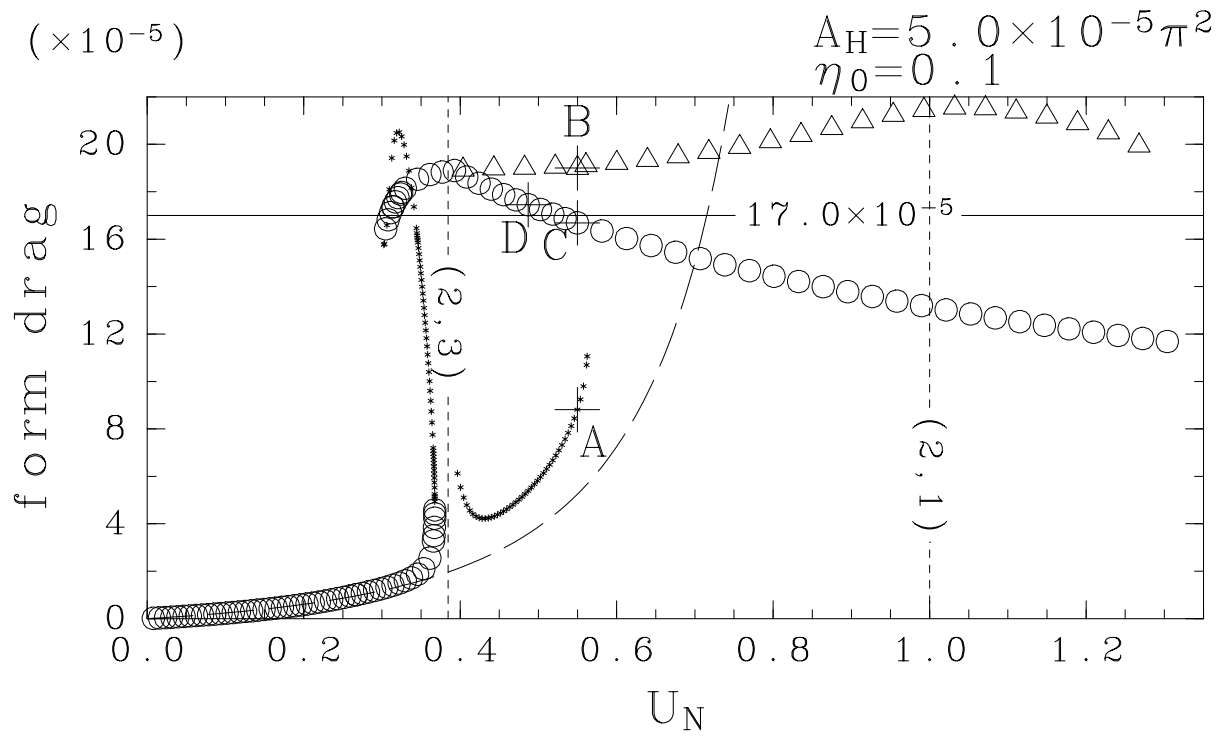


Figure 9: Form drag of steady solutions obtained by the LMM in the high-order model. $\eta_0 = 0.1$, $A_H = 5.0 \times 10^{-5} \pi^2$. \circ : stable, \triangle : unstable to only odd modes, $*$: unstable to even modes. A broken line is the linear one. For the letter 'A', 'B', 'C' and 'D', see text. The solid line of 17.0×10^{-5} is referred in chapter 4.

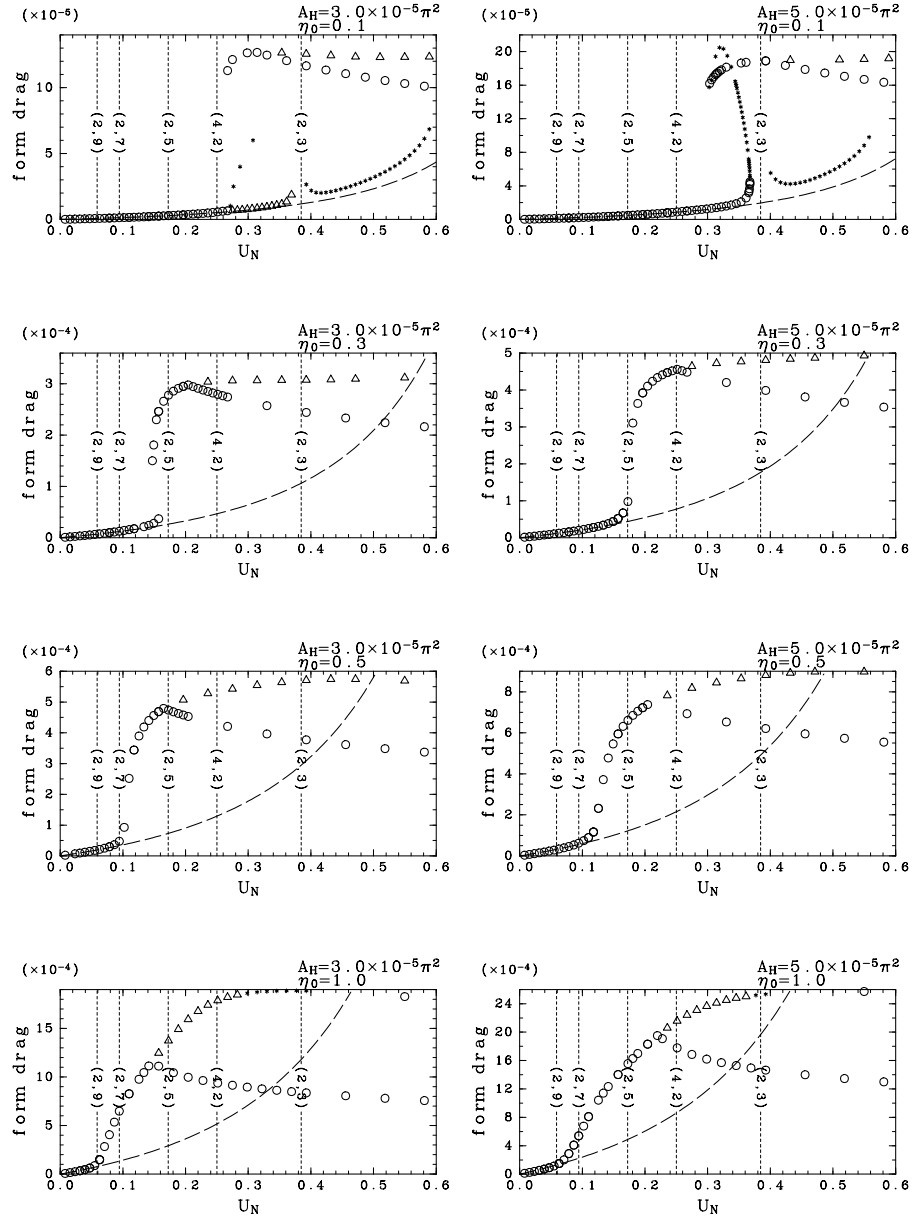


Figure 10: Form drag of steady solutions obtained by the LMM. Symbols are same as in Fig. 9. First row: $\eta_0 = 0.1$, second row: $\eta_0 = 0.3$, third row: $\eta_0 = 0.5$ and fourth row: $\eta_0 = 1.0$. Left four panels: $A_H = 3.0 \times 10^{-5} \pi^2$, and right four panels: $A_H = 5.0 \times 10^{-5} \pi^2$.

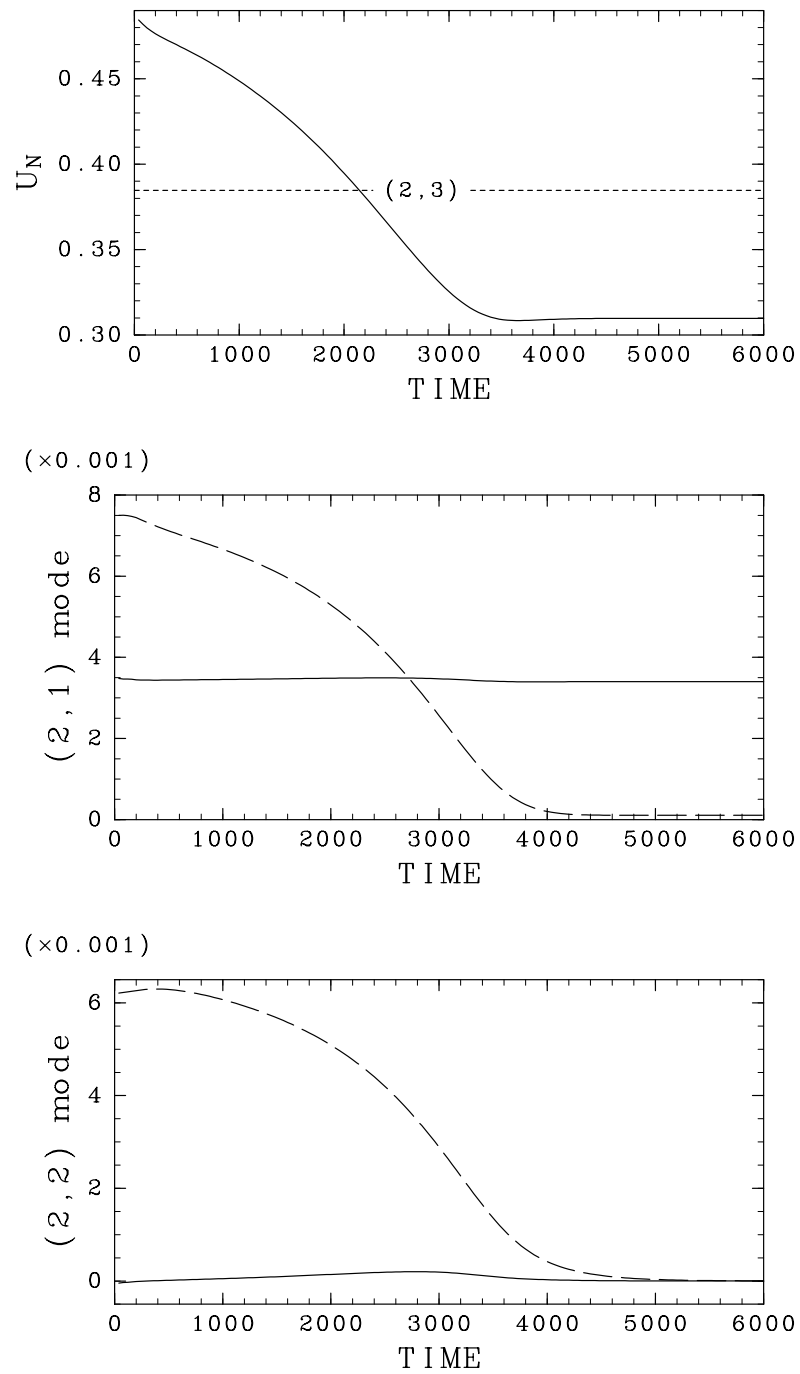


Figure 11: The example of the form drag instability. Time series of U_N (the uppermost panel), the $(2,1)$ mode (the middle panel), which is a even mode, and the $(2,2)$ mode (the lowest panel), which is a odd mode, are shown starting from the solution 'D' in Fig. 9 when $\tau = 1.7 \times 10^{-4}$. In the middle and the lowest panels, the solid line denotes a cosine component and the broken line denotes a sine component.

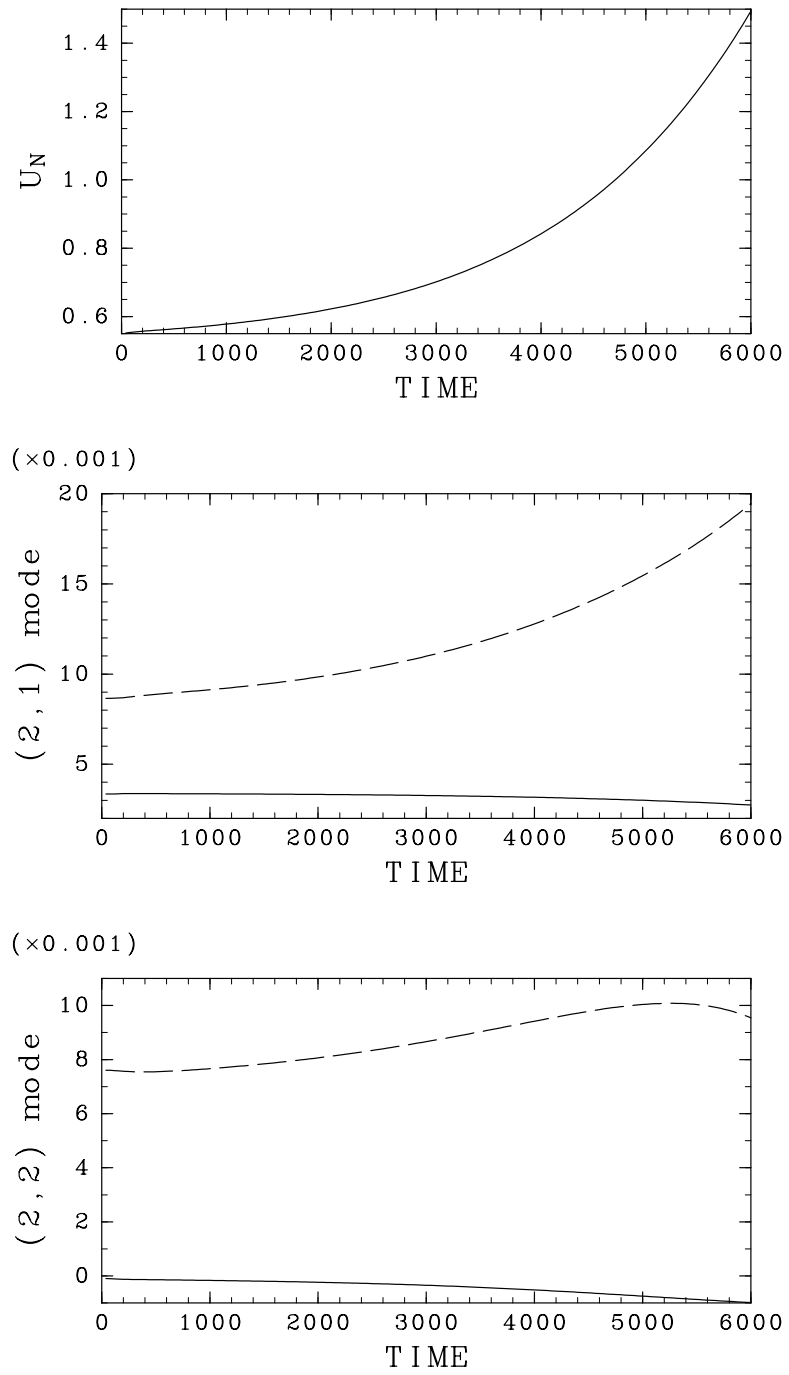


Figure 12: Same as Fig. 11 but for starting from the solution 'C' in Fig. 9.

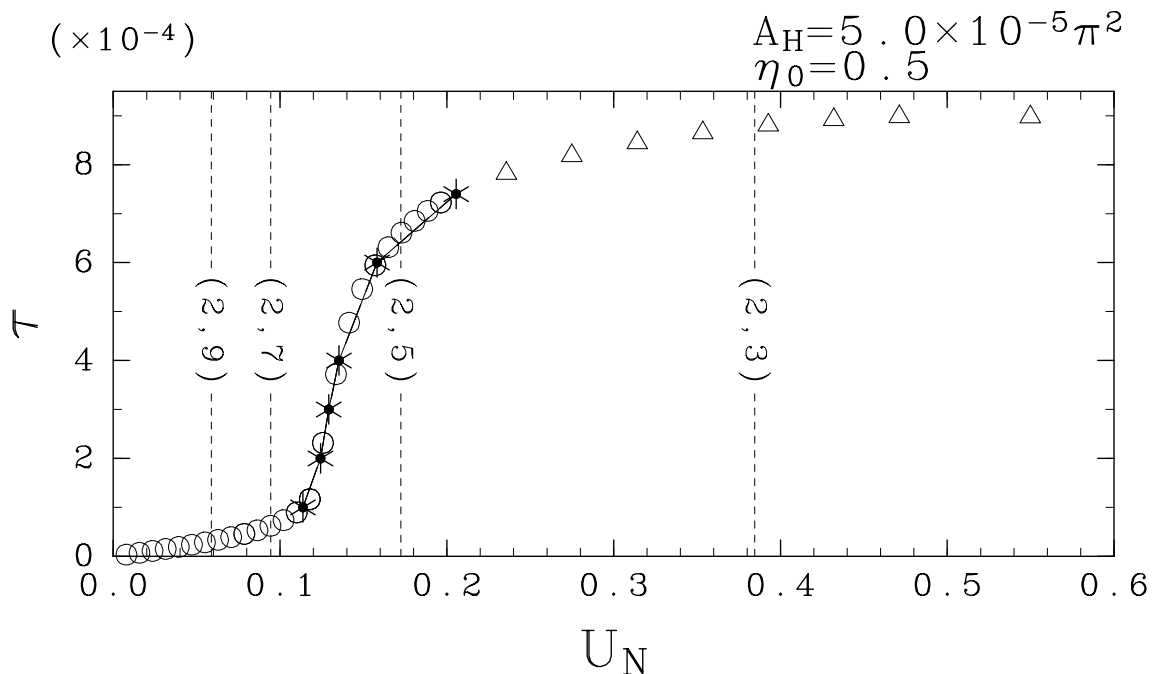
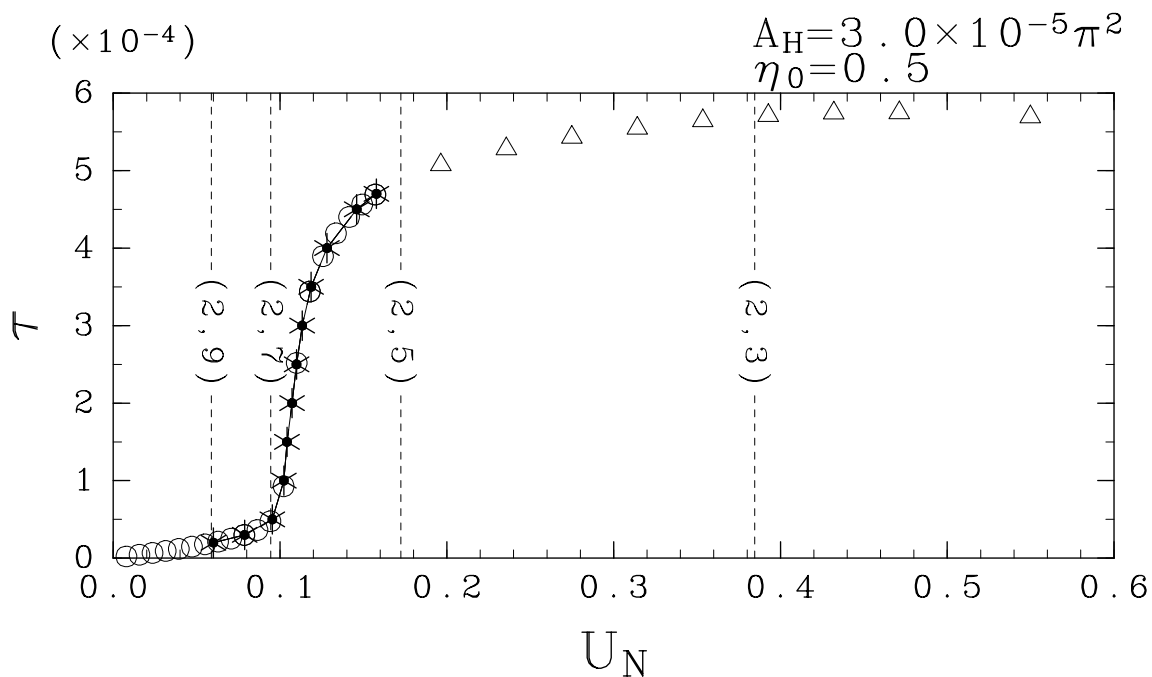


Figure 13: The solutions of the numerical experiments when $\eta_0 = 0.5$. The steady solutions that the solutions of the experiments converge into are plotted by *. \circ and \triangle are solutions obtained by the LMM (same as in Fig. 10; \circ : stable and \triangle : unstable to only odd modes). Asymmetric stable solutions are not plotted (see Fig. 10). The upper panel: $A_H = 3.0 \times 10^{-5} \pi^2$, the lower panel: $A_H = 5.0 \times 10^{-5} \pi^2$.

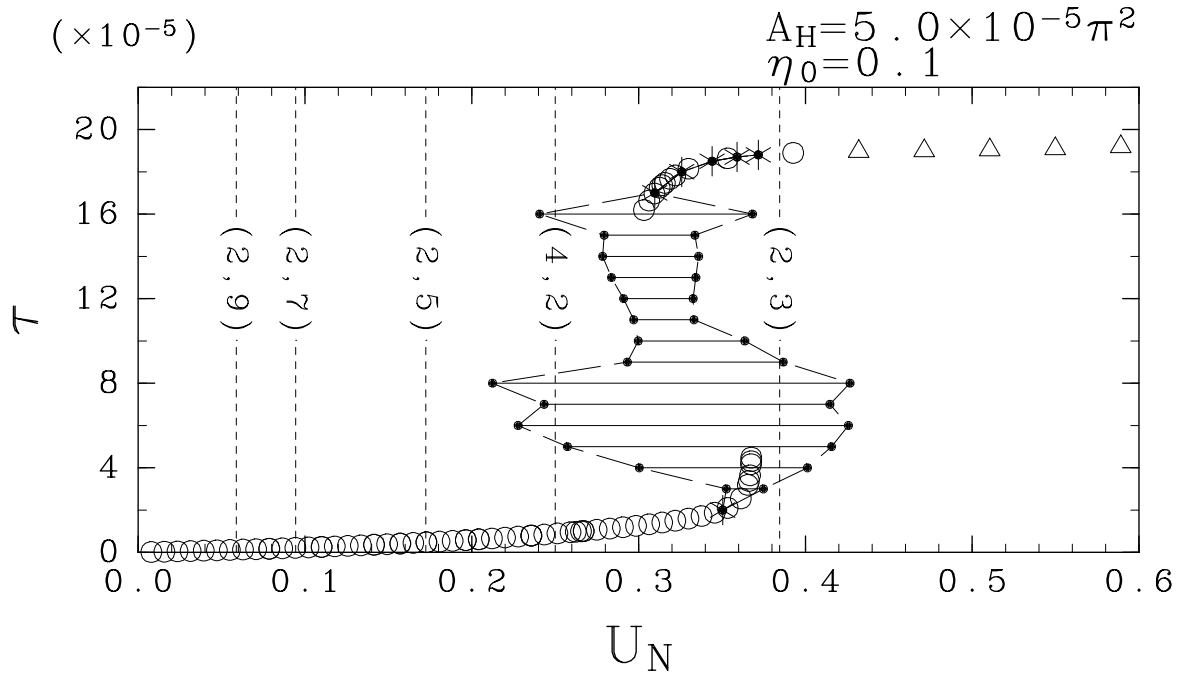
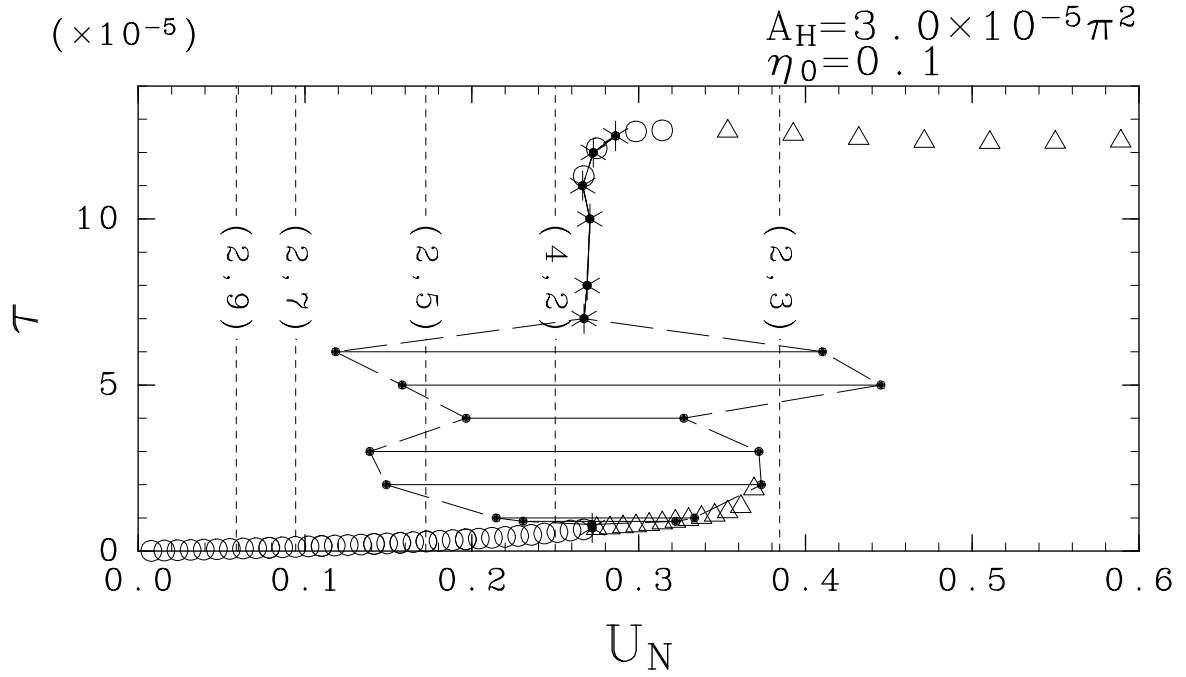


Figure 14: The solutions of the numerical experiments. Cases that the time-dependent solution does not converge are denoted by a pair of \bullet connected by a solid line. A pair of \bullet denote the maximum and the minimum U_N . Other symbols are same as in Fig. 13. $\eta_0 = 0.1$. The upper panel: $A_H = 3.0 \times 10^{-5} \pi^2$, the lower panel: $A_H = 5.0 \times 10^{-5} \pi^2$.

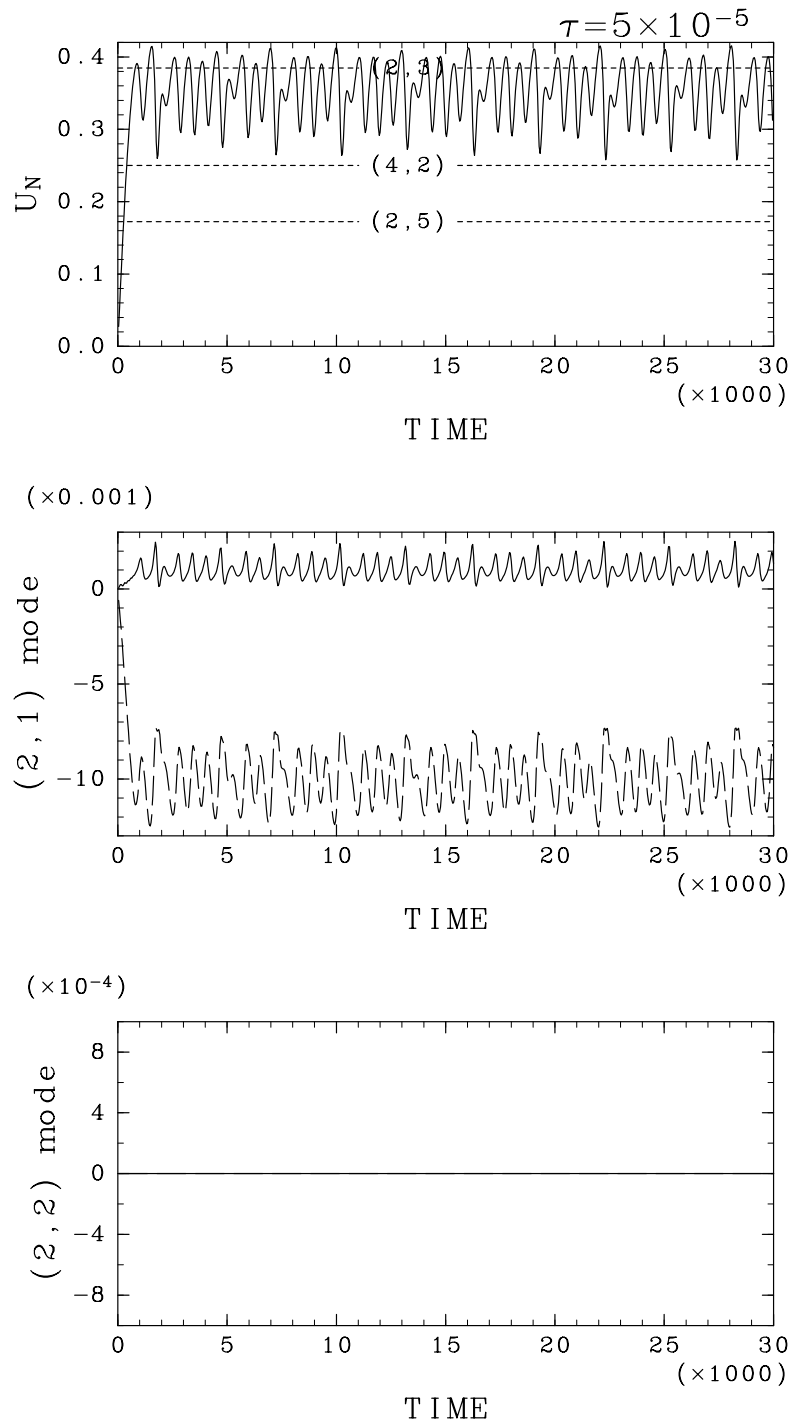


Figure 15: An example of the oscillatory solution in which even modes are dominate. Time series of U_N (the uppermost panel), the (2,1) mode (the middle panel), which is a even mode, and the (2,2) mode (the lowest panel), which is a odd mode, are shown when $(\eta_0, A_H) = (0.1, 5.0 \times 10^{-5} \pi^2)$ and $\tau = 5.0 \times 10^{-5}$. In the middle and the lowest panel, the solid line denotes a cosine component and the broken line denotes a sine component.

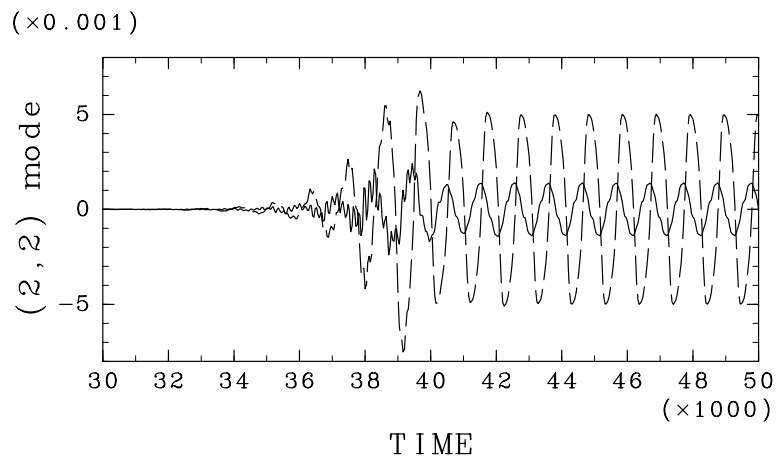
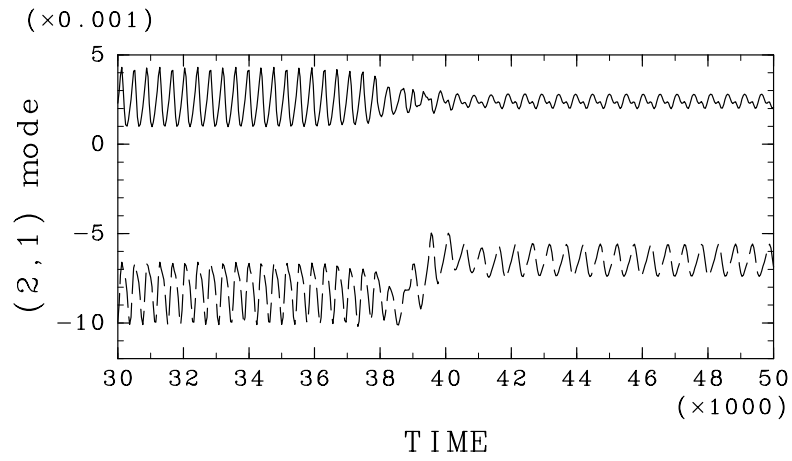
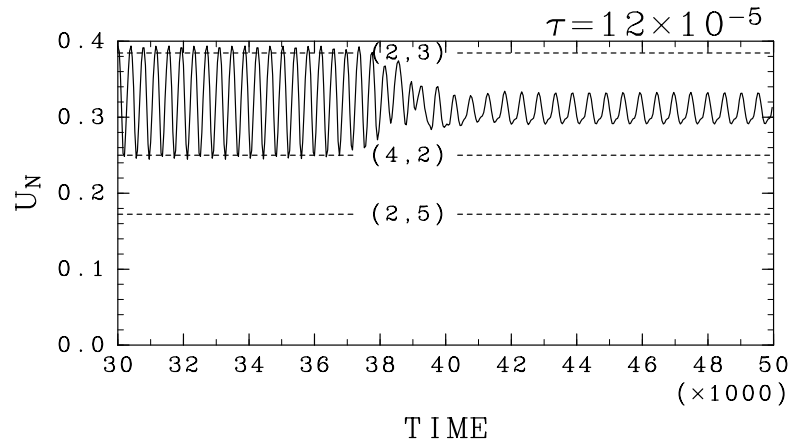


Figure 16: Same as Fig. 15 but for $\tau = 1.2 \times 10^{-4}$. And the scale of the horizontal axis is not the same as Fig. 15.

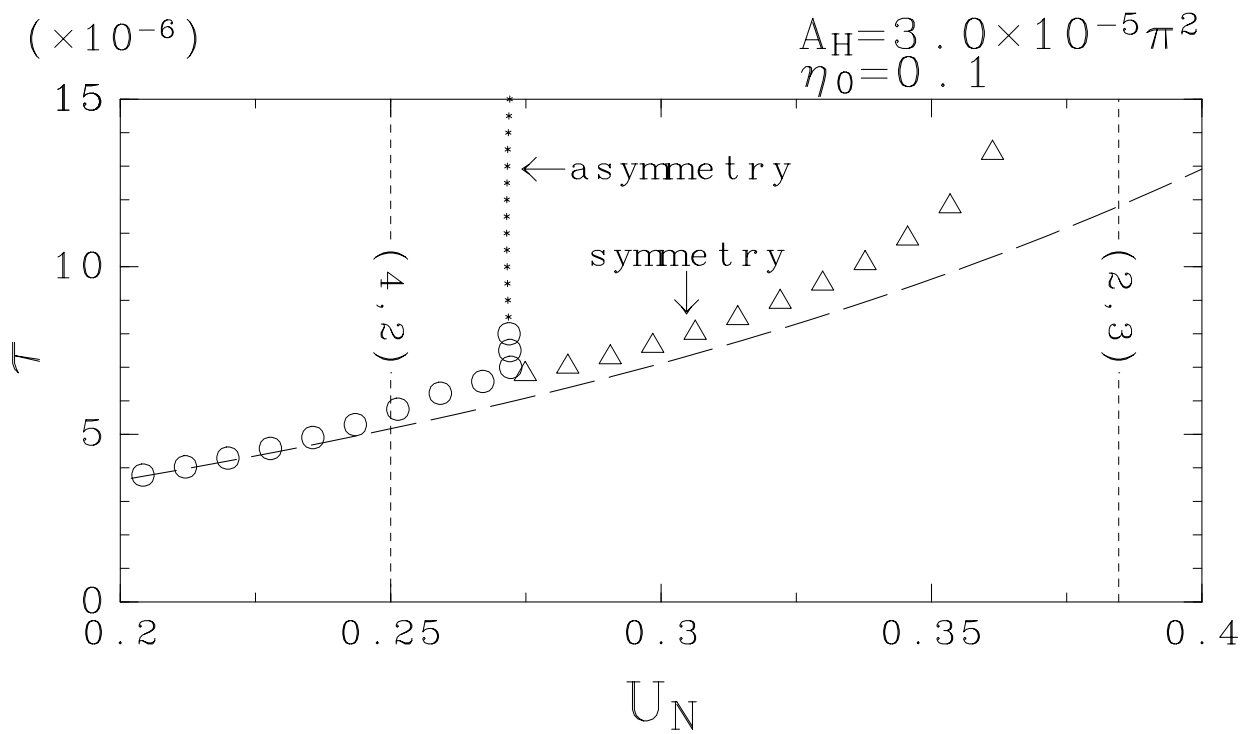


Figure 17: The steady solutions near the bifurcation along the quasi-linear solution in the case of $(\eta_0, A_H) = (0.1, 3.0 \times 10^{-5} \pi^2)$. The symbols are same as Fig. 9, but the stability is calculated by treating U_N as a variable unlike in Fig. 9.

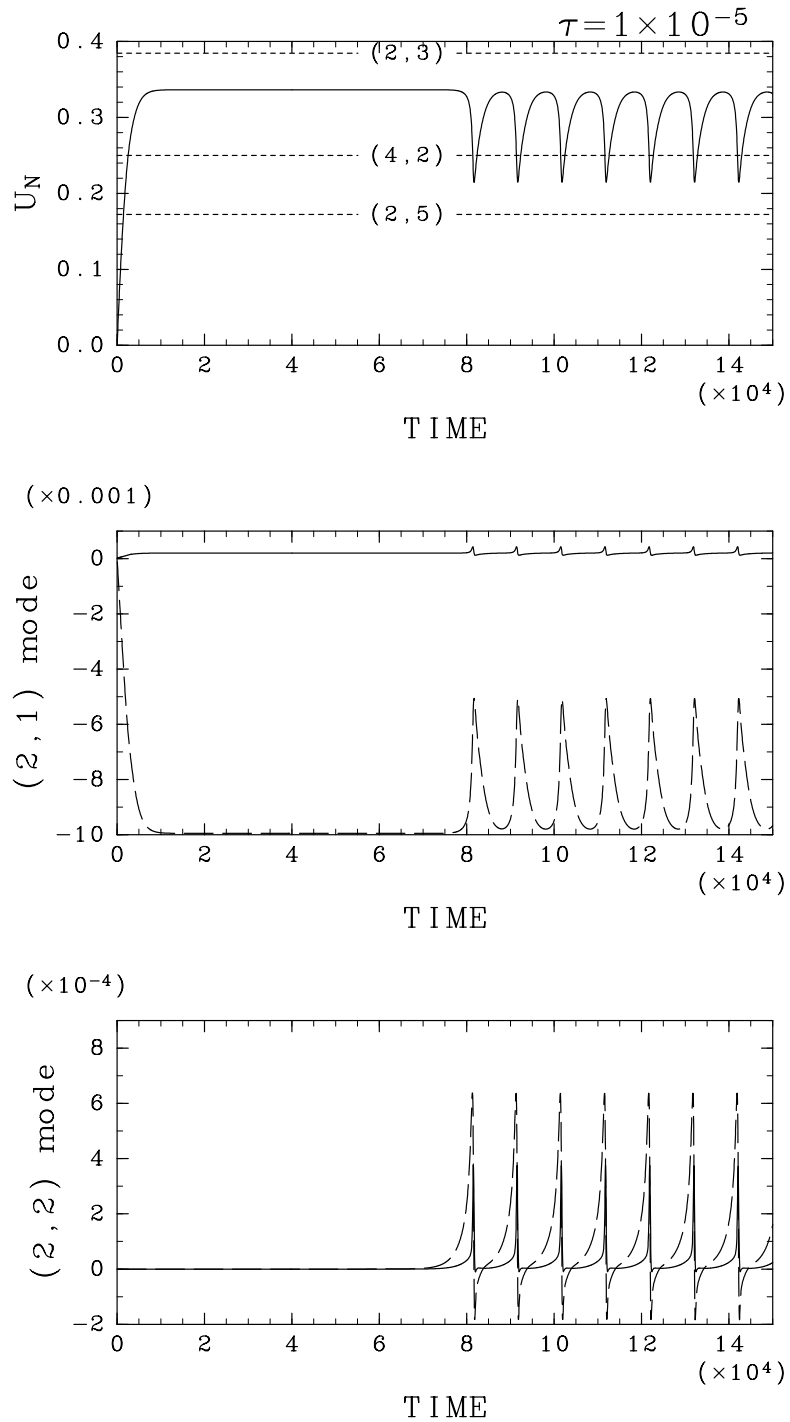


Figure 18: Same as Fig. 15 but for $(\eta_0, A_H) = (0.1, 3.0 \times 10^{-5} \pi^2)$ and $\tau = 1.0 \times 10^{-5}$. And the scale of the horizontal axis is not the same as Fig. 15.

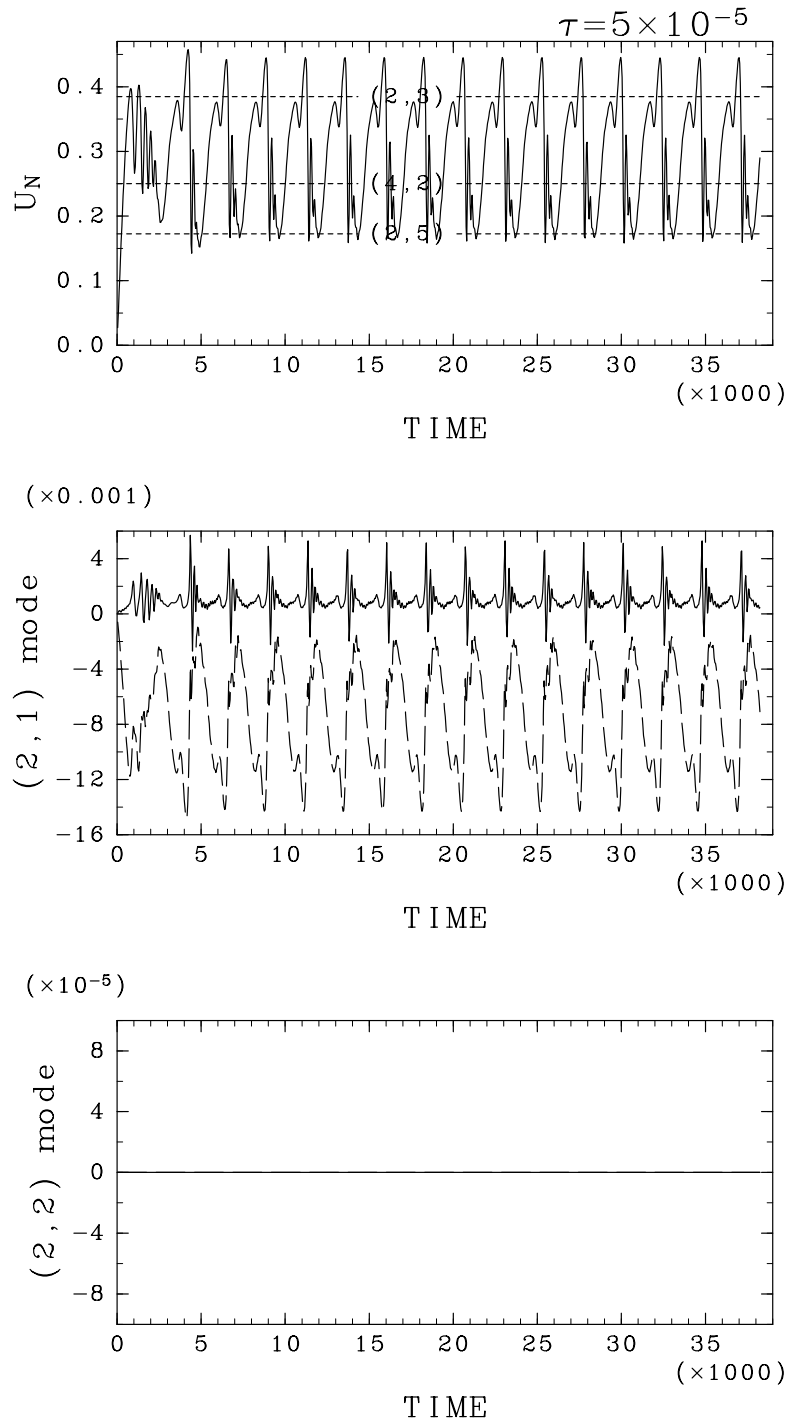


Figure 19: Same as Fig. 15 but for $(\eta_0, A_H) = (0.1, 3.0 \times 10^{-5} \pi^2)$ and $\tau = 5.0 \times 10^{-5}$. And the scale of the horizontal axis is not the same as Fig. 15.

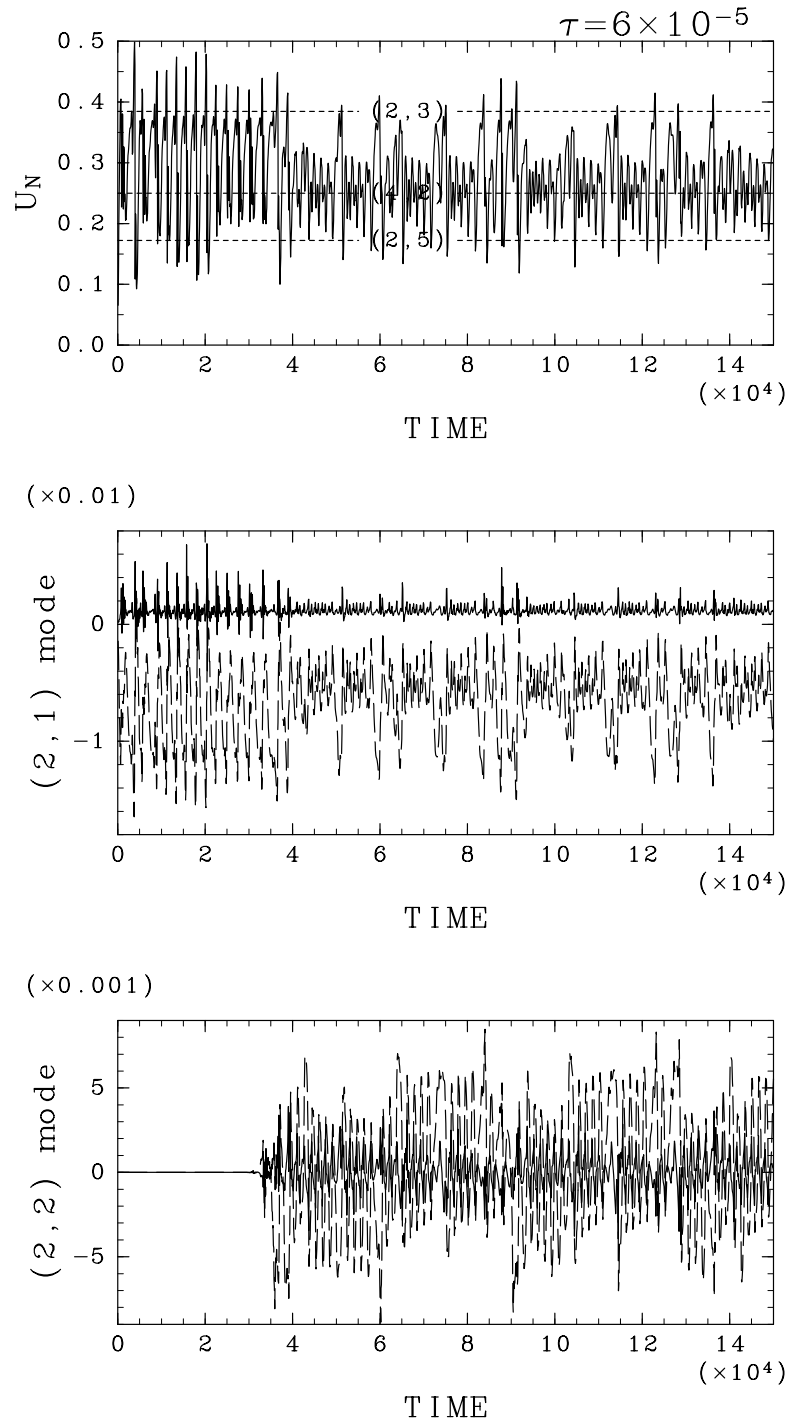


Figure 20: Same as Fig. 15 but for $(\eta_0, A_H) = (0.1, 3.0 \times 10^{-5} \pi^2)$ and $\tau = 4.0 \times 10^{-5}$. And the scale of the horizontal axis is not the same as Fig. 15.

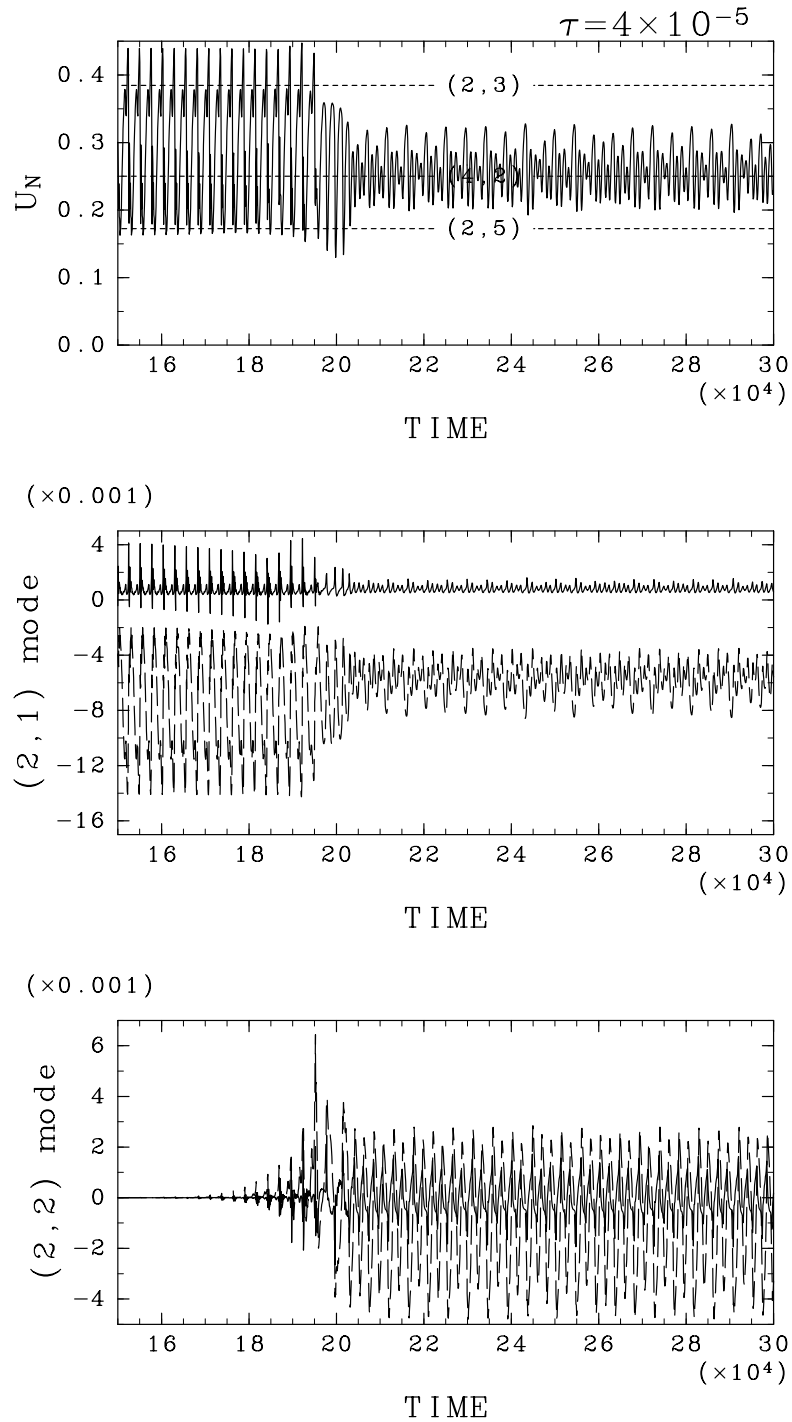


Figure 21: Same as Fig. 15 but for $(\eta_0, A_H) = (0.1, 3.0 \times 10^{-5} \pi^2)$ and $\tau = 4.0 \times 10^{-5}$. And the scale of the horizontal axis is not the same as Fig. 15.

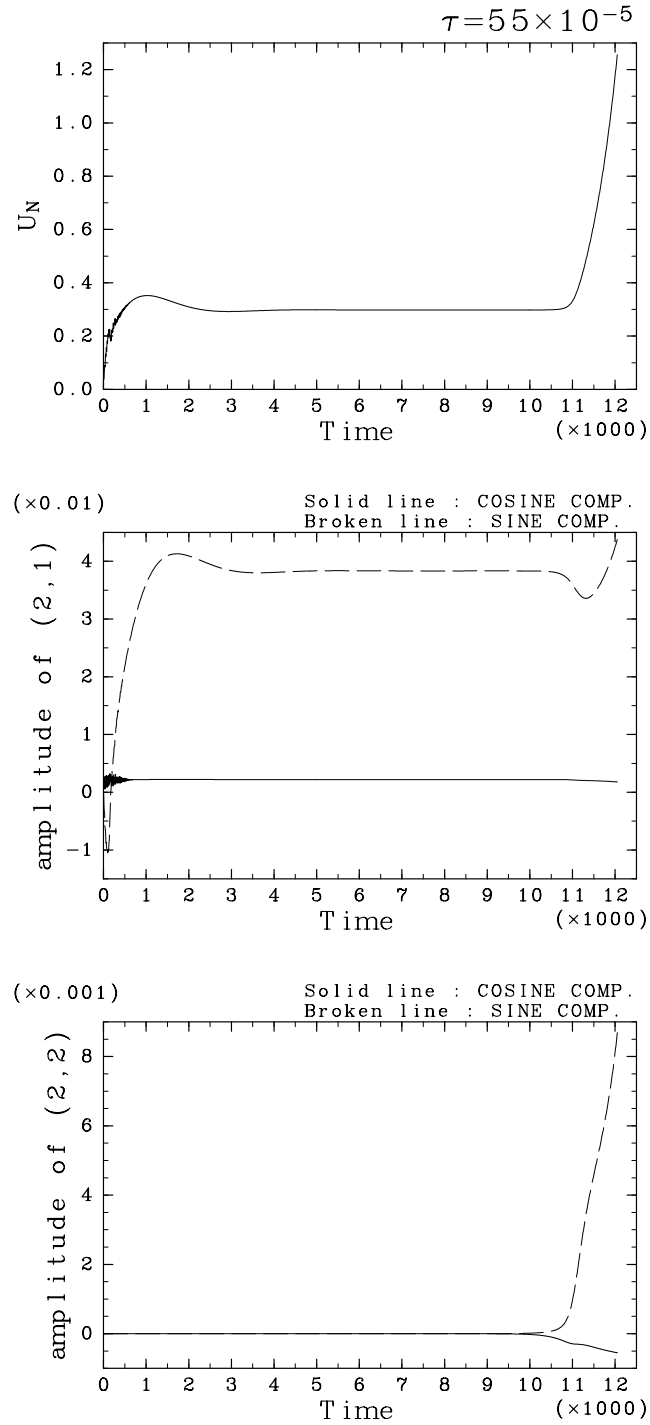


Figure 22: The trajectories when $\tau = 5.5 \times 10^{-4}$ in the case of $(\eta_0, A_H) = (0.5, 3.0 \times 10^{-5} \pi^2)$, the same case as the upper panel in Fig. 13. The acceleration once stops but restarts after odd modes grow ($t \simeq 11000$). The uppermost panel: time series of U_N . The middle panel: time series of the coefficients of (2,1), which is an even mode. The lowest panel: time series of the coefficients of (2,2), which is an odd mode.

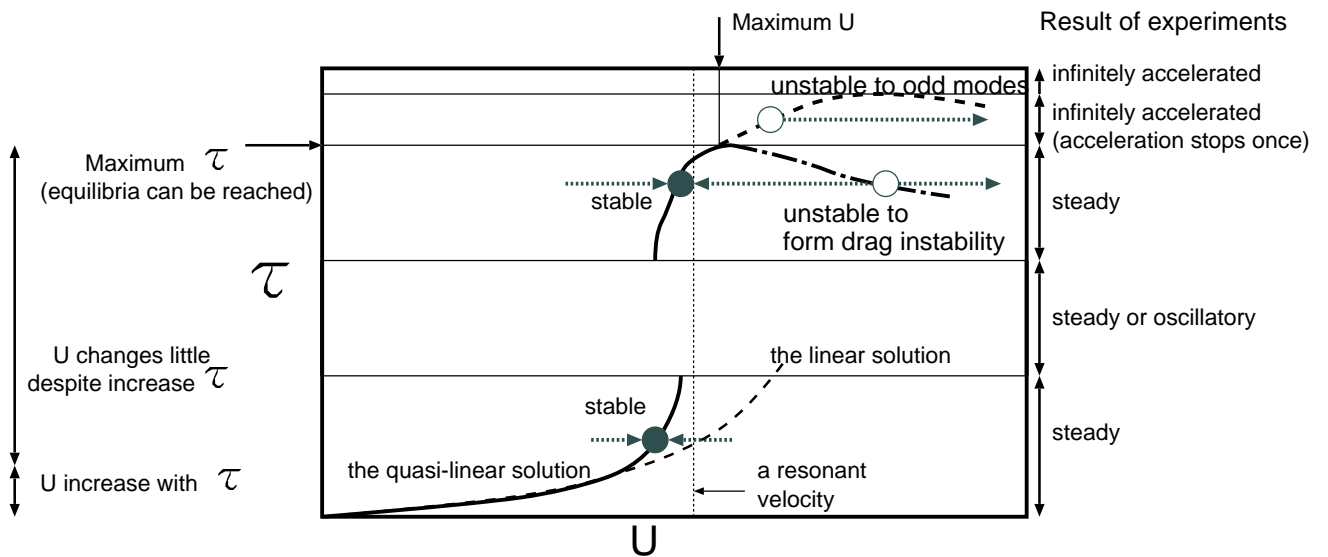


Figure 23: Schematic diagram of the solutions. The vertical axis is τ and the horizontal axis is U_N .

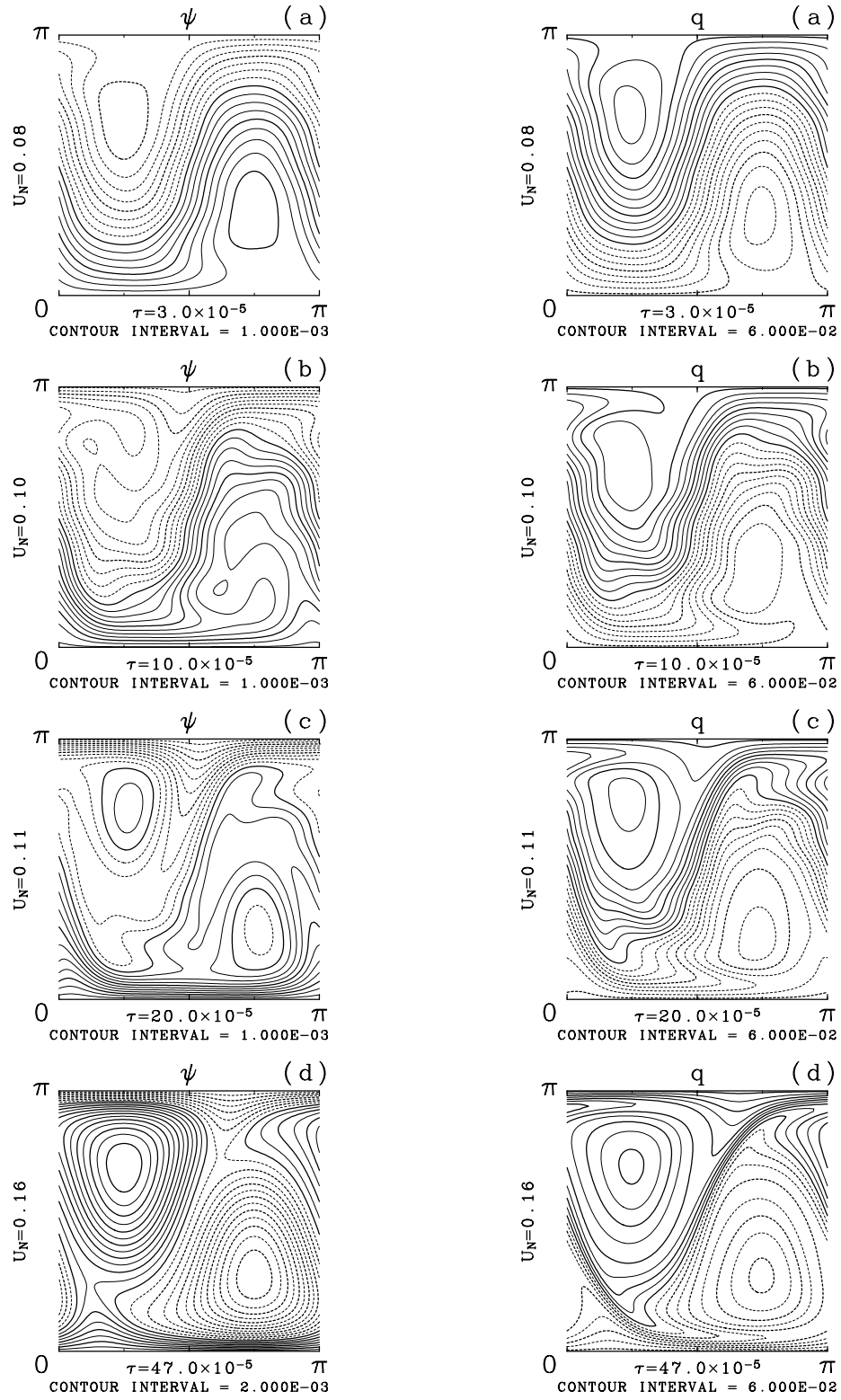


Figure 24: Contours of the stream function(ψ) and the potential vorticity(q). The first row (a): $\tau = 3.0 \times 10^{-5}$, the second row (b): $\tau = 1.0 \times 10^{-4}$, the third row (c): $\tau = 2.0 \times 10^{-4}$, the forth row (d): $\tau = 4.7 \times 10^{-4}$. $(\eta_0, A_H) = (0.5, 3.0 \times 10^{-5} \pi^2)$. Solid contours correspond to plus values and dotted contours to minus values.

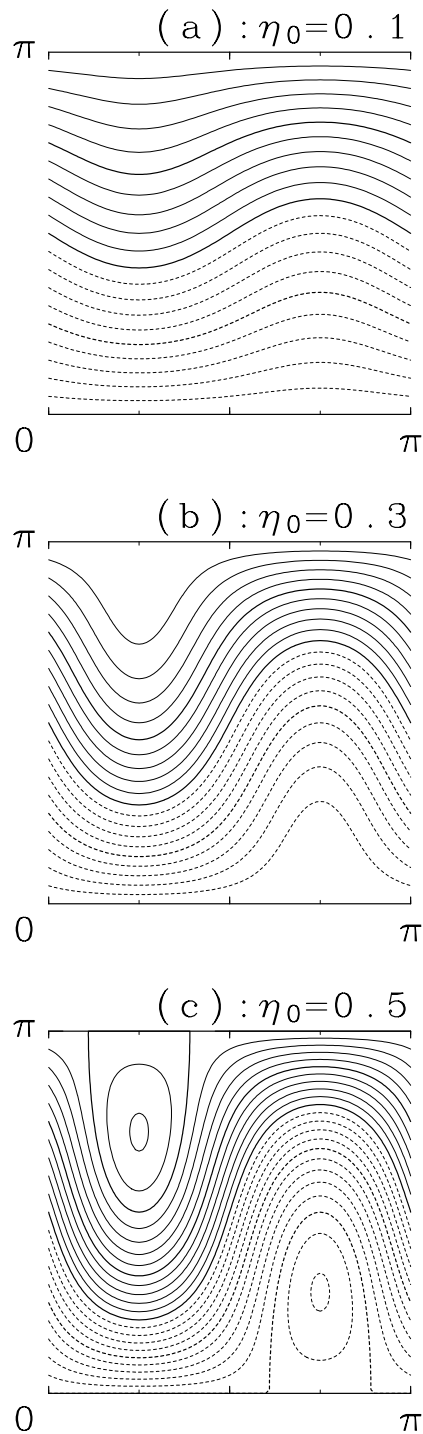


Figure 25: The ambient potential vorticity contour. (a): $\eta_0 = 0.1$, (b): $\eta_0 = 0.3$, (c): $\eta_0 = 0.5$. The contour interval is 5.0×10^{-2} in any case.

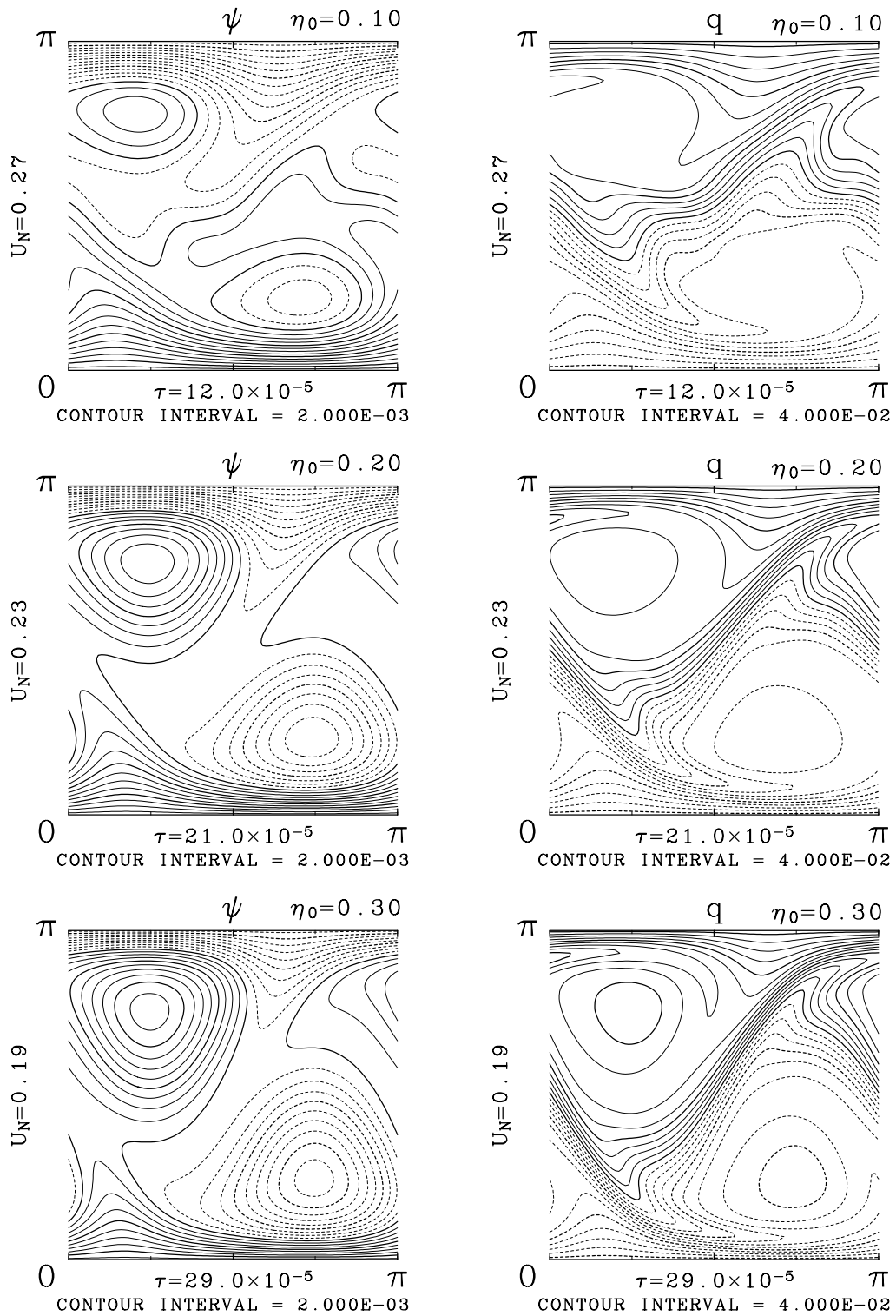


Figure 26: Contours of the stream function(ψ) and the potential vorticity(q) of the largest τ with which the steady states are reached. The uppermost : $\eta_0 = 0.1$, the middle : $\eta_0 = 0.2$, the lowest: $\eta_0 = 0.3$. $A_H = 3.0 \times 10^{-5} \pi^2$.